Geochemistry, Geophysics, Geosystems®

RESEARCH ARTICLE
10.1029/2025GC012729

Geochemical Analysis of Diachronous V-Shaped Ridges and Troughs That Flank the Reykjanes Ridge South of Iceland

Nicky White[1], Chia-Yu Tien[1], Callum Pearman[1], John Maclennan[1], Bramley Murton[2], and Expedition 395 Scientists[3]

[1]Bullard Laboratories, Department of Earth Sciences, University of Cambridge, Cambridge, UK, [2]National Oceanography Centre, Southampton, UK, [3]International Ocean Discovery Program, Texas A&M University, College Station, TX, USA

Key Points:

- We present geochemical analyses of whole-rock samples from boreholes drilled into V-shaped ridges and troughs that flank the Reykjanes Ridge, south of Iceland
- Combined inverse and forward modeling of major, trace and rare earth element concentrations reveals temperature differences of 25–30°C from ridge to trough
- These results rule out some competing hypotheses and contribute to an elucidation of the fluid dynamics of horizontal flow within the head of a major convective upwelling

Supporting Information:

Supporting Information may be found in the online version of this article.

Correspondence to:

N. White and C.-Y. Tien,
njw10@cam.ac.uk;
cyt28@cam.ac.uk

Citation:

White, N., Tien, C.-Y., Pearman, C., Maclennan, J., Murton, B., & Expedition 395 Scientists (2026). Geochemical analysis of diachronous V-shaped ridges and troughs that flank the Reykjanes Ridge south of Iceland. *Geochemistry, Geophysics, Geosystems*, *27*, e2025GC012729. https://doi.org/10.1029/2025GC012729

Received 6 OCT 2025
Accepted 25 FEB 2026

Author Contributions:

Conceptualization: Nicky White, Chia-Yu Tien
Funding acquisition: Nicky White, Bramley Murton
Investigation: Bramley Murton

Abstract It is recognized that mantle plumes play a direct role in generating regional uplift and producing immense volumes of basaltic magmatism, both of which can influence paleoclimate. The Icelandic Plume, beneath the North Atlantic Ocean, is of particular importance due to its size and position at a significant paleoceanographic gateway. It is transected by a mid-oceanic ridge system, which has generated a series of V-shaped ridges and troughs that flank the Reykjanes Ridge south of Iceland. The origin of these diachronous features is debated—do they reflect thermal fluctuations within the plume head or have they formed as a result of compositional variations within the buoyant convecting mantle? To address these and other hypotheses, the International Ocean Discovery Program (IODP) carried out three drilling expeditions, which recovered basalt cores from a sequence of V-shaped ridges and troughs. Here, we show that the petrology and geochemistry of fifty whole-rock samples taken from boreholes that penetrate different ridges and troughs reveal systematic differences in major, trace and rare earth element concentrations. By combining forward and inverse modeling based upon polybaric fractional melting, we show that these geochemical variations can be explained by varying melt fraction as a function of depth for plausible mantle source compositions. Our results suggest that temperature differences of 25–30°C between cooler troughs and hotter ridges play a dominant role. We conclude that the drilled basaltic rocks reveal a chronology of resolvable temperature perturbations that should help to elucidate the fluid dynamics of flow within this major plume.

Plain Language Summary Beneath the North Atlantic Ocean, immense amounts of hot material rise up beneath Iceland from deep within Earth's mantle, forming a gigantic pancake-shaped upwelling. This upwelling, known as the Icelandic mantle plume, is the largest on Earth and plays a key role in determining the depth and shape of the North Atlantic Ocean over distances of thousands of kilometers. A pattern of distinctive V-shaped ridges and troughs that are hundreds of kilometers long and tens of kilometers wide occur on the seabed south of Iceland. These V-shaped ridges are thought by many scientists to have been generated by waxing and waning of the plume, but their exact origin is still hotly debated. Here, we analyze lava flows from these ridges and troughs that were drilled during three ambitious seagoing expeditions. Chemical differences between these flows can be used to estimate the temperature of the plume as it evolves. The story is a complicated one but it is probable that small temperature changes of 25–30°C are needed to explain our chemical observations. Our results have important implications for the history of ancient oceanic circulation which may be controlled by the fluctuating plume.

1. Introduction

It is generally recognized that the Icelandic Plume, a major convective upwelling within the mantle, is one of the largest on Earth (Hoggard et al., 2020). Apart from its size, three additional factors make this plume worthy of detailed study. First, it is transected by a slow spreading mid-oceanic ridge (MOR), which acts as a linear window into its transient thermal behavior during Neogene and, arguably, Paleogene times. A quantitative understanding of this transience is likely to yield important fluid dynamical insights about mantle convection in general and upwelling plumes in particular. Second, the Icelandic Plume is positioned at a globally significant oceanic gateway between Greenland and Western Europe across which North Atlantic Deep Water (NADW) flows. It has long been argued that vertical motions triggered by transient radial plume flow act to modulate overflow of NADW and its ancient precursor, Northern Component Water (Abelson et al., 2008; Poore et al., 2006; Wright & Miller, 1996). Finally, there is mounting evidence that continental margins, which fringe the North Atlantic Ocean, have suffered repeated transient uplift events. Some of these events appear to have generated ephemeral

Methodology: Nicky White, Chia-Yu Tien, Callum Pearman, John Maclennan
Project administration: Nicky White
Software: Chia-Yu Tien
Supervision: Nicky White, John Maclennan
Visualization: Nicky White, Chia-Yu Tien
Writing – original draft: Nicky White
Writing – review & editing: Chia-Yu Tien, Callum Pearman, John Maclennan

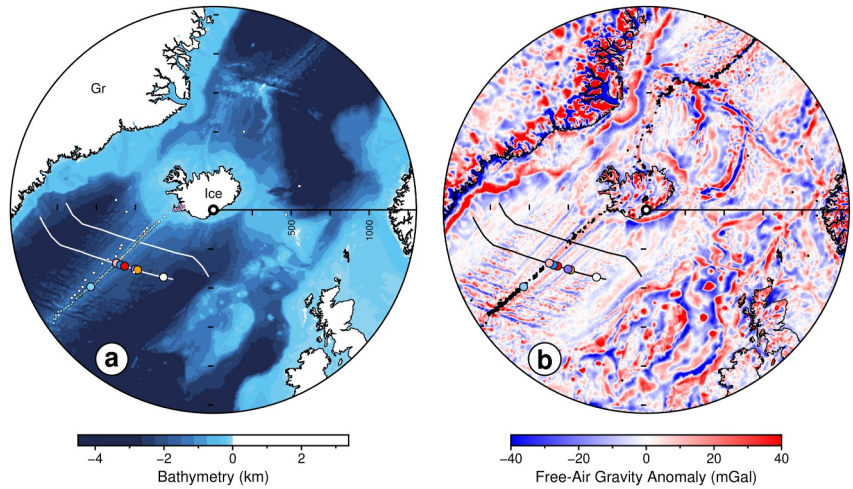

Figure 1. Bathymetric and Free-Air Gravity Maps. (a) Bathymetric map of North Atlantic Ocean constructed using ETOPO1 database (Amante & Eakins, 2009). Large white circle with thick black rim = center of radial polar projection located at Vatnajökull, which is surface expression of putative plume conduit (Shorttle et al., 2010); black line with tick marks and other tick marks indicate radial distances in km from plume conduit; seven large colored and white circles = loci of drill sites from IODP Expeditions 384/395C/395; small white circles = loci of dredged glass and whole rock samples from mid-oceanic ridge (Jones et al., 2014; Murton et al., 2002) and from legacy DSDP/ODP drill sites; small turquoise circles = loci of dredged/drilled samples for which rare earth element analyses exist and for which MgO >7.5 wt.% (Jones et al., 2014; Murton et al., 2002); small plum circles = field samples from Peate et al. (2009) for which rare earth element analyses exist and for which MgO > 7.0 wt.% (see Figure 5); pair of white flowlines = seismic reflection profiles described by Parnell-Turner et al. (2017); Ice = Iceland; Gr = Greenland. (b) Short wavelength free-air gravity anomalies (Sandwell & Smith, 2009). Small black circles = loci of earthquakes with magnitudes >4 (1968–2008; Engdahl et al., 2020); other lines and symbols as in panel (a).

landscapes at times that coincide with anomalous global warming events (e.g., PETM, ETM-2, ETM-3; Conway-Jones & White, 2022).

The clearest manifestation of temporal activity are the so-called V-shaped ridges and troughs that flank the mid-oceanic ridges on either side of Iceland. These diachronous features were first described by Vogt (1971) and are best observed on either side of the Reykjanes Ridge, south of Iceland. Limited seismic wide-angle and reflection studies have been used to constrain the crustal structure of Neogene and Paleogene V-shaped ridges and troughs. In combination with free-air gravity and aeromagnetic observations, it has been suggested that ridges and troughs are underlain by thicker and thinner oceanic crust, respectively (R. S. White et al., 1995).

There is an ongoing debate about the origin of these V-shaped ridges and troughs: Are they generated by radial flow away from the plume center or by channelized flow along the MOR itself? Do they represent thermal and/or compositional variations within the underlying asthenosphere? The range of hypotheses includes the influence of propagating rift effects at the MOR itself and of buoyant wet mantle upwellings (Hey et al., 2010; Martinez & Hey, 2017). The best way to address these different questions is by combining geophysical and geochemical measurements within the context of a fluid dynamical understanding of plume behavior. For example, the detailed velocity structure of oceanic crust along both axial and flow lines will yield important constraints upon the cumulative volume of basaltic melt generated beneath the MOR as a function of time. Concentrations of major, trace and rare earth elements combined with isotopic measurements will help to determine the depth and extent of isentropic melting as well as heterogeneity of the mantle source region.

Here, we focus our attention upon a single aspect of this general problem—the petrologic and geochemical analysis of whole-rock basalt samples obtained from combined International Ocean Discovery Program (IODP) Expeditions 384/395C/395 (Figure 1). One objective of these expeditions was to recover basalt core from off-axis, and therefore buried, V-shaped troughs and ridges. Previous studies focussed upon dredged basaltic glasses and rocks recovered along the Reykjanes Ridge and upon a small number of off-axis samples of weathered basalt dredged from the crests of the youngest V-shaped ridges (Jones et al., 2014; Murton et al., 2002; Schilling, 1973). During the drilling expeditions, basalt core was recovered from five different sites (Figure 1). At four

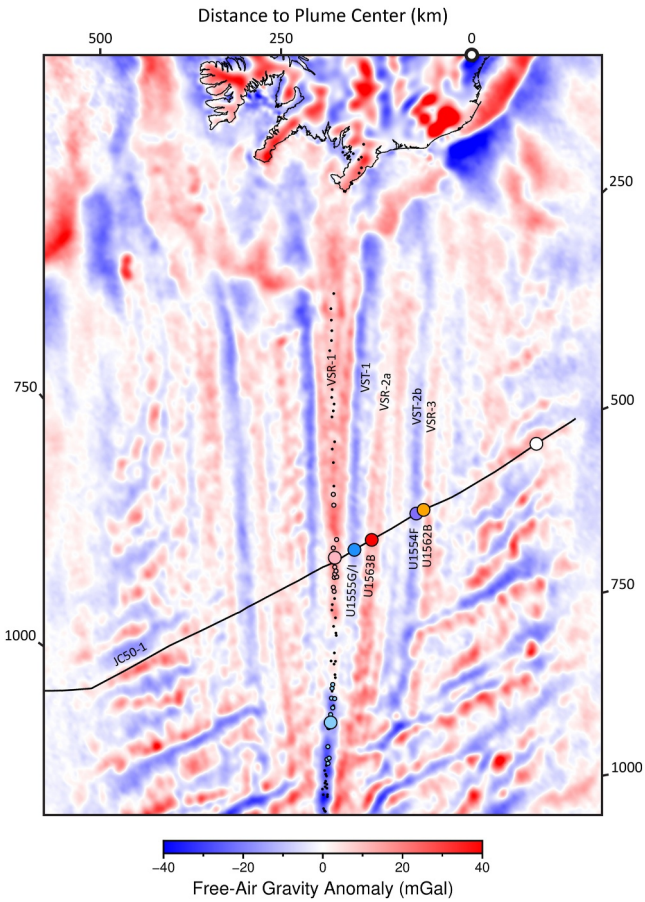

Figure 2. Geometry of V-Shaped Ridges. Detailed map of short wavelength free-air gravity anomalies where V-shaped ridges and troughs are manifest by positive (red) and negative (blue) anomalies (see Poore et al. (2009) for nomenclature). Radial polar projection where numbers along edges indicate radial distance from putative plume center indicated by white circle with thick black rim along upper boundary. Large turquoise/pink circles = average loci of V-shaped trough/ridge pair along zero-age mid-oceanic ridge; blue/red circles = loci of younger pair of drill sites; purple/orange circles = loci of older pair of drill sites; white circle = locus of oldest drill site not considered here; smaller turquoise/pink circles = loci of dredged glass and whole-rock analyses used to calculate average compositions at large turquoise/pink circles (Jones et al., 2014; Murton et al., 2002); small black circles = loci of selected samples dredged from mid-oceanic ridge and collected from Reykjanes Peninsula (see Figure 1); labeled black line = regional seismic reflection profile JC50-1 from Parnell-Turner et al. (2017).

of these sites (U1555, U1563, U1554 and U1562), boreholes penetrated two pairs of V-shaped troughs and ridges and at a fifth site one borehole penetrated much older fractured oceanic crust where influence of the Icelandic Plume is thought to have been negligible based upon legacy crustal thickness measurements (Figure 2). This fifth site is not considered in this contribution (Pearman et al., 2026).

This observational and modeling study is focussed upon basaltic rocks recovered from two pairs of troughs and ridges. A complementary study of glass samples is presented elsewhere (Pearman et al., 2026). Our goals are threefold. First, we present petrologic and geochemical observations from boreholes at each of the four sites. A significant part of this goal is to show how these observations relate to previously acquired observations from the active Reykjanes Ridge itself. Second, we carry out polybaric melting calculations in order to determine the depth and extent of melting at each borehole location. The centerpiece of each calculation is combined forward and inverse modeling of major, trace and rare earth elements for a range of putative mantle sources. Third, we compare our results with a selection of independent geophysical constraints and outline the significance of our results for the fluid dynamics of those mantle convective processes that might operate within the radially spreading horizontal layer of a major hot upwelling.

2. Petrologic Setting

The location of each borehole along the JC50-1 seismic reflection profile that was acquired along a flowline parallel to the plate spreading direction is shown in Figure 3 (Parnell-Turner et al., 2017). Detailed descriptions of operational procedures and of the recovered basaltic rocks are available in the relevant IODP reports (Parnell-Turner et al., 2022, 2024, 2025). Here, a brief summary of the principal lithologies encountered at each site provides the context for subsequent sampling, geochemical analysis and modeling (Figure 4). Original descriptions are based upon a combination of detailed macroscopic observations of core samples, microscopic thin section observations, and physical property measurements (e.g., core scans, magnetic susceptibility, color reflectance, wireline logs).

2.1. Site U1555

Site U1555 is positioned on the youngest V-shaped trough, VST-1, where the estimated basement age is 2.8 Ma (Figures 3b and 4; Parnell-Turner et al., 2025). The most significant holes, located 20 m apart from each other, are 384-U1555G (75 m of core with 43% recovery) and 395C-U1555I (105 m of core with 48% recovery). Both of these holes were sampled which provides 20 analyses from this site. These two holes are dominated by coherent sheet flows interspersed with fragmented pillow lavas (Figure 4). Minor amounts of basalt were recovered from Holes 384-U1555F and 395C-U1555H (6.5 and 0.4 m recovered, respectively) but are not considered in this contribution.

2.2. Site U1563

Site U1563 is located on the first off-axis V-shaped ridge, VSR-2a, where the estimated basement age is 5.2 Ma. Rock coring at Hole 395C-U1563B reached a depth of ~456 m CSF-A (~154 m into basement) with 28.6% recovery (Figure 4). This hole is dominated by fragmented pillow basalts with relatively few sheet flows. Minor amounts of basaltic pillow fragments and breccia (<1 m) were also recovered in the last 2 cores of Hole 395C-

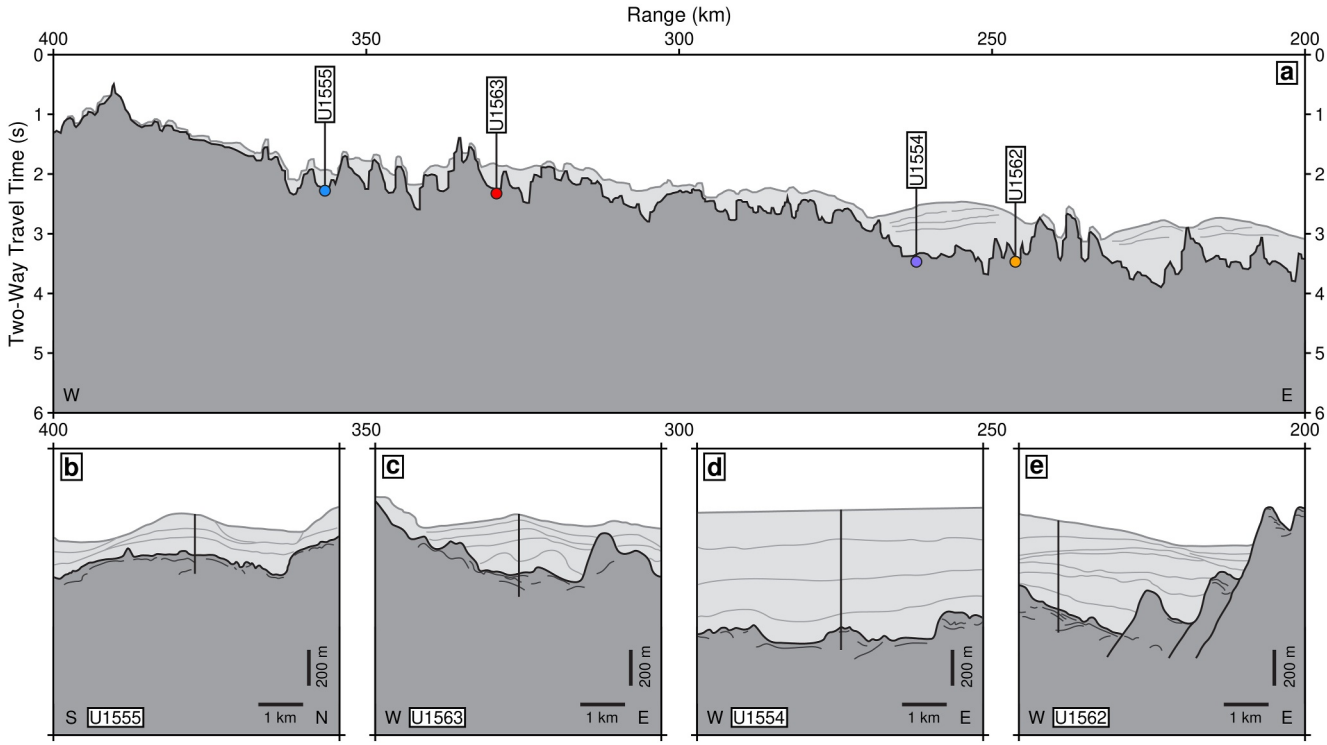

Figure 3. Seismic Reflection Profiles. (a) Schematic interpretation of eastern portion of seismic reflection flowline JC50-1 redrawn from Parnell-Turner et al. (2017). Dark gray shading = acoustic basement (i.e., oceanic crust); light gray shading with thin lines = contourite drift deposits and their internal structure; black line = sediment-basement interface; labeled colored circles = drill sites from IODP Expeditions 384 and 395C as before. On the vertical axis, 1 s represents 0.75 km within water column and 3 km within crust. (b–e) Detailed interpretation at each drill site redrawn from Parnell-Turner et al. (2022). Vertical black lines = drill holes with indicative depths of penetration; continuous black line = sediment-basement interface; discontinuous black lines = bright reflections within oceanic basement; inclined black lines = normal faults; shading as before.

U1563A. Intercalated sedimentary and peperitic layers occur throughout Hole 395C-U1563B, making up nearly 15% of the recovered material.

2.3. Site U1554

The next V-shaped trough, VST-2b, was drilled at Site U1554 where oceanic basement is 12.7 million years old. Significant quantities of minor to moderately altered basalt with a depth of penetration of 130 m and a recovery of >60% were obtained from Hole U1554F, yielding 80 m of core. One meter of basalt was drilled at Hole U1554E. The contact between the overlying sedimentary strata and basalt is not directly sampled in either hole. Igneous rock cores from this site are dominated by pillow lava intervals, which are often fragmented, and coherent sheet flow intervals (Figure 4). Thin layers of intercalated baked calcareous mudstone and peperite occur throughout the top one third of the sequence.

2.4. U1562

Site U1562 is positioned along the western side of the next V-shaped ridge, VSR-3, which has an estimated basement age of 13.9 Ma. Hole 395C-U1562B was drilled to a depth of 133 m into basement with a recovery of 48%. Glassy pillow lava fragments and the top of a weathered flow sheet were recovered from the base of Hole 395C-U1562A. The sediment-basement contact is poorly exposed. This site comprises approximately equal amounts of sparsely to moderately olivine phyric pillow lavas and sheet flows.

3. Geochemical Analysis

Our sampling strategy is guided by two considerations. First, we wish to analyze the freshest possible samples which were identified during the process of core description and logging. Second, we wish to analyze a large

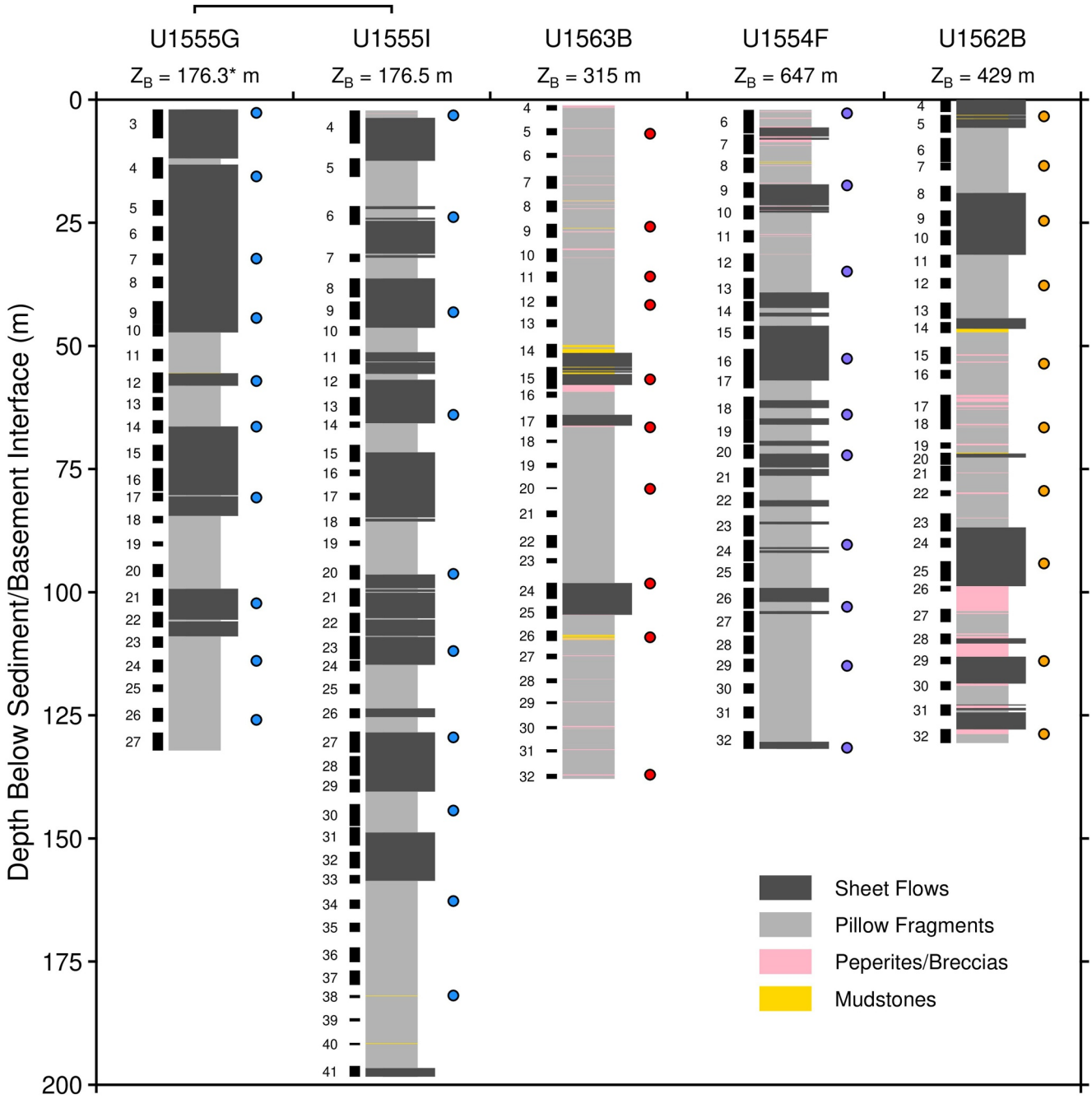

Figure 4. Schematic Logs of Basalt Lithology. Five simplified lithologic logs from four drill sites that summarize principal rock types, core recovery, and whole-rock sample locations where Site U1555 has two drill holes located ~20 m apart. Note that these logs are slightly modified versions of original shipboard logs and core descriptions (Parnell-Turner et al., 2025). In each case, depth is plotted from the sediment-basement interface and Z_B is thickness of overlying sedimentary section. Dark gray rectangles = interpreted sheet flow units; light gray rectangles = fragmentary pillow units; pink rectangles = peperites and lava breccias; yellow rectangles = thin mudstone units that are occasionally baked; numbered black rectangles along left-hand edge of each log indicate core recovery where number refers to core identifier; circles = color-coded whole-rock sample locations.

number of samples with uniform spatial coverage. A total of 50 whole-rock samples were selected at ~10 m intervals from the two ridge-trough pairs, which yields a reasonably even coverage for each hole (Tables 1–5). At this stage, we are less concerned with lithologic differences although pillow basalt fragments and sheet flows are approximately equally sampled throughout. Note that Site U1555 comprises two deep holes but only analyses from U1555G are presented here.

Table 1
Analyses for Hole U1555G (60°13.68490′ N, 28°29.99970′ W)

Depth CSF-A (m)	178.99	191.90	208.57	220.66	233.42	242.70	257.09	278.55	290.25	302.22
Major Elements from XRF (wt.%)										
SiO_2	50.8	50.7	50.3	49.8	50.3	50.0	49.8	50.2	50.3	50.0
TiO_2	1.1	1.1	1.1	1.1	1.1	1.1	1.1	1.1	1.1	1.1
Al_2O_3	14.0	14.0	14.1	14.1	14.1	13.9	13.9	13.9	14.0	13.9
Fe_2O_{3T}	11.9	12.5	12.3	12.3	12.3	12.2	12.3	12.5	12.6	12.1
MnO	0.17	0.19	0.18	0.17	0.18	0.18	0.18	0.19	0.19	0.18
MgO	8.04	8.55	8.38	8.63	8.58	8.52	8.59	8.99	8.78	8.79
CaO	11.7	11.7	11.7	11.7	11.6	11.5	11.6	11.6	11.7	11.4
Na_2O	1.74	1.74	1.81	1.79	1.82	1.69	1.68	1.71	1.73	1.75
K_2O	0.1	0.05	0.06	0.06	0.05	0.08	0.08	0.09	0.04	0.06
P_2O_5	0.09	0.08	0.09	0.08	0.08	0.08	0.08	0.08	0.08	0.08
LOI	0.27	0.10	0.13	0.12	0.48	0.060	0.020	0.24	0.15	0.29
Total	100	101	100	99.9	101	99.3	99.3	101	101	99.7
Minor and Trace Elements from XRF (ppm)										
Sc	43.3	43.2	43.3	40.1	41.8	41.5	41.4	41.4	40.8	45.1
V	332	330	328	316	324	320	321	323	325	326
Cr	380	378	392	375	402	404	413	401	380	422
Ni	137	134	137	129	148	161	159	148	144	167
Cu	90.3	88.8	90.4	86.9	88.2	87.1	86.2	88.3	87.4	88.2
Zn	87.6	88.0	88.2	79.9	87.4	88.7	88.6	87.4	85.7	91.3
Sr	67.2	66.3	67.8	67.4	64.8	65.2	64.5	63.7	66.4	64.0
Y	28.6	28.9	29.1	28.3	29.0	28.6	28.6	28.8	28.9	28.6
Zr	56.7	56.3	56.9	53.3	53.7	54.9	54.9	54.0	55.3	53.1
Nb	1.9	1.8	1.8	1.7	1.7	1.6	1.6	1.7	1.8	1.8
Pb	0.5	0.6	0.5	0.4	0.7	0.8	0.5	0.4	0.7	0.4
Trace Elements from ICP-MS (ppm)										
Ga	16.5	16.8	16.2	16.5	15.2	16.5	17.9	16.5	16.6	16.9
Rb	1.83	0.758	0.864	0.946	0.534	1.07	0.991	1.05	0.722	0.911
Cs	0.045	0.0084	0.017	0.0058	0.015	0.014	0.015	0.016	0.011	0.017
Ba	9.24	9.21	11.0	11.8	8.31	8.96	7.82	7.08	8.55	6.53
La	1.87	1.85	1.88	1.77	1.78	1.84	1.76	1.78	1.72	1.71
Ce	5.88	5.85	5.93	5.68	5.75	5.91	5.63	5.55	5.50	5.48
Pr	1.08	1.06	1.10	1.05	1.06	1.09	1.04	1.02	1.01	1.03
Nd	6.22	6.12	6.29	6.08	6.40	6.25	6.05	5.82	5.93	5.87
Sm	2.35	2.43	2.41	2.44	2.39	2.46	2.40	2.38	2.45	2.46
Eu	0.893	0.899	0.932	0.904	0.958	0.957	0.920	0.920	0.923	0.936
Gd	3.33	3.39	3.48	3.35	3.52	3.52	3.53	3.45	3.50	3.53
Tb	0.692	0.691	0.723	0.688	0.721	0.737	0.714	0.727	0.740	0.733
Dy	4.98	4.87	5.05	4.81	5.06	5.14	4.97	5.05	5.10	5.08
Ho	1.03	1.07	1.09	1.05	1.09	1.11	1.07	1.10	1.12	1.11
Er	2.98	3.02	3.14	3.05	3.18	3.22	3.15	3.18	3.19	3.16
Tm	0.474	0.468	0.494	0.473	0.485	0.510	0.497	0.492	0.493	0.496

Table 1
Continued

Depth CSF-A (m)	178.99	191.90	208.57	220.66	233.42	242.70	257.09	278.55	290.25	302.22
Yb	3.04	2.94	3.10	2.99	3.10	3.11	3.08	3.14	3.13	3.12
Lu	0.463	0.461	0.488	0.453	0.477	0.483	0.470	0.480	0.484	0.471
Hf	1.71	1.68	1.76	1.68	1.70	1.75	1.72	1.68	1.73	1.71
Ta	0.109	0.111	0.112	0.112	0.109	0.107	0.107	0.0975	0.100	0.100
Th	0.113	0.114	0.115	0.110	0.111	0.115	0.102	0.107	0.109	0.101
U	0.072	0.055	0.057	0.046	0.049	0.059	0.040	0.045	0.052	0.056

Major, trace and rare earth element analyses were carried out on all 50 whole-rock samples (Figures 5 and 6). Major element concentrations were analyzed using a Philips PW2404 wavelength-dispersive sequential X-ray fluorescence spectrometer (XRF) at the School of GeoSciences, University of Edinburgh. Trace element concentrations were analyzed using a Perkin Elmer Nexion 350D quadrupole inductively coupled plasma mass spectrometer (ICP-MS) at the Department of Earth Sciences, University of Cambridge. Analytical methods for XRF and ICP-MS together with their standard protocols are described in detail by Fitton et al. (1998) and by Gibson et al. (2005), respectively.

Comparison of our different analyses with legacy data sets from the zero-age Reykjanes Ridge and from the onshore Reykjanes Peninsula forms an important aspect of our study (Figure 1). Along the Reykjanes Ridge, we exploit the body of analyses assembled by Murton et al. (2002) and by Jones et al. (2014). In both cases, these measurements were carried out upon a combination of whole-rock samples and glasses. On the Reykjanes Peninsula itself, we refer to whole-rock analyses carried out by Peate et al. (2009).

3.1. Major Elements

Figure 5a shows a Total Alkali Silica (TAS) diagram together with a series of variation diagrams where different elements are plotted as a function of MgO. Samples from zero-age, young and old V-shaped ridges and troughs lie in the sub-alkaline field. Trough samples have systematically higher alkali and lower silica values whereas ridge samples show the opposite. Note that ridge samples appear to extend into the basaltic andesite field, which may reflect post-eruptive secondary alteration since glass analyses are confined to the basalt field (Pearman et al., 2026).

Variation diagrams reveal that MgO varies between 7.5 and 10 wt.%. Calculated Mg numbers vary between 53 and 66, indicating that these basalts are primitive. There are small but systematic differences in Mg number from troughs to ridges: 56.6–60.9 (U1555G and I) and 58.6–66.0 (U1563B); 52.6–54.6 (U1554F) and 62.9–64.6 (U1562B). From the perspective of major element systematics, these differences may reflect either changes in the depth and degree of melting, minor variations in mantle source composition, or some combination of both. The extent of cooling and crystallization also play a significant role which requires careful correction. Despite scatter, the observed trends suggest that the principal control for major element distribution is fractional crystallization.

Al_2O_3 and CaO diagrams show that there are weak linear trends as a function of MgO for several of the V-shaped troughs (e.g., VST-1, VST-2b), which are indicative of principally olivine fractionation rather than clinopyroxene and/or plagioclase fractionation. The Na_2O diagram is revealing and significant because it shows a systematic relationship between Na_2O concentrations and ridge/trough geometry. Thus for a given value of MgO (e.g., 9 wt.%), higher and lower values of Na_2O are associated with troughs and ridges, respectively. This inverse relationship is particularly clear for the young ridge-trough pair, which has very similar values of MgO. These Na_2O values are generally typical of MORB rocks and glasses dredged from the North Atlantic mid-oceanic ridge (Gale et al., 2013, 2014). Finally, the TiO_2 diagram has a similar pattern, although anomalously elevated values are observed for Hole U1554F. Samples from this hole also have a large range of elevated K_2O values.

Figures 6d and 6g show average major elemental concentrations for each hole normalized with respect to Primitive Mantle. Three important observations can be made which confirm what the different variation diagrams reveal. First, average values of major elements are narrowly constrained with little evidence for significant downhole variation. The one exception concerns Hole U1562B where there is a change in chemical composition

Table 2
Analyses for Hole U1555I (60°13.68966′N, 28°29.99842′W)

Depth CSF-A (m)	179.71	200.35	219.64	240.47	272.78	288.45	305.96	320.83	339.22	358.39
Major Elements from XRF (wt.%)										
SiO_2	50.3	50.0	49.5	50.2	50.6	49.5	49.5	49.2	49.1	49.2
TiO_2	1.1	1.1	1.1	1.1	1.1	1.1	1.1	1.1	1.1	1.1
Al_2O_3	14.1	13.9	13.9	13.9	13.7	13.6	13.7	13.6	14.1	14.5
Fe_2O_{3T}	12.2	12.3	12.4	12.6	12.2	12.4	12.3	12.5	12.3	11.4
MnO	0.18	0.18	0.18	0.18	0.18	0.18	0.18	0.18	0.17	0.17
MgO	8.06	8.47	8.39	8.67	8.83	9.17	8.75	8.88	8.97	8.96
CaO	11.8	11.6	11.5	11.7	11.3	11.1	11.5	11.4	11.3	11.6
Na_2O	1.76	1.71	1.73	1.74	1.72	1.76	1.71	1.77	1.81	1.87
K_2O	0.08	0.08	0.08	0.08	0.08	0.07	0.08	0.07	0.07	0.07
P_2O_5	0.09	0.08	0.09	0.08	0.08	0.08	0.08	0.08	0.08	0.08
LOI	0.92	0.58	0.60	0.49	0.070	1.2	1.1	0.93	1.1	1.1
Total	101	100	99.3	101	100	100	100	99.7	100	100
Minor and Trace Elements from XRF (ppm)										
Sc	44.3	42.6	41.2	39.7	43.1	38.3	39.5	42.1	44.2	46.5
V	336	328	323	321	323	309	317	317	330	352
Cr	380	382	371	378	422	387	401	395	421	452
Ni	130	139	128	138	169	159	164	158	172	170
Cu	90.0	88.3	85.8	85.6	88.1	81.8	85.1	85.0	91.0	94.3
Zn	88.4	86.7	82.2	83.0	90.7	80.1	88.4	93.8	91.2	95.1
Sr	66.3	65.9	68.6	65.2	63.5	63.1	64.2	64.8	64.3	68.4
Y	29.3	28.9	28.7	28.8	28.3	27.8	28.4	28.2	28.7	28.7
Zr	56.8	56.0	56.2	54.7	53.4	51.2	53.1	52.6	53.3	53.4
Nb	1.7	1.8	1.8	1.5	1.7	1.5	1.7	1.7	1.7	1.8
Pb	0.7	0.3	0.5	0.2	0.5	0.6	0.8	0.3	0.4	0.5
Trace Elements from ICP-MS (ppm)										
Ga	15.7	14.9	15.9	15.7	15.8	15.0	16.3	15.8	14.9	16.2
Rb	1.13	0.693	0.526	0.619	1.40	0.987	0.943	0.532	1.38	1.03
Cs	0.013	0.013	0.011	0.017	0.014	0.017	0.024	0.0042	0.014	0.0092
Ba	7.89	7.68	9.80	7.05	12.7	9.67	6.31	8.59	9.09	10.3
La	1.78	1.76	1.79	1.74	1.68	1.61	1.64	1.62	1.70	1.63
Ce	5.72	5.57	5.67	5.61	5.39	5.17	5.18	5.14	5.44	5.35
Pr	1.04	1.01	1.06	1.04	0.960	0.951	0.977	0.959	0.995	0.987
Nd	6.13	5.94	6.14	5.98	5.79	5.62	5.53	5.72	5.75	5.81
Sm	2.31	2.32	2.41	2.36	2.34	2.33	2.28	2.24	2.40	2.33
Eu	0.906	0.921	0.940	0.928	0.899	0.870	0.878	0.876	0.871	0.919
Gd	3.35	3.34	3.43	3.53	3.30	3.28	3.29	3.24	3.36	3.25
Tb	0.687	0.705	0.722	0.725	0.704	0.679	0.700	0.686	0.704	0.713
Dy	4.86	4.78	4.99	4.97	4.97	4.76	4.83	4.76	4.83	4.95
Ho	1.07	1.07	1.08	1.08	1.06	1.05	1.05	1.07	1.06	1.07
Er	3.02	3.06	3.11	3.12	3.04	3.02	3.08	3.03	3.09	3.04
Tm	0.489	0.481	0.493	0.481	0.470	0.474	0.479	0.472	0.486	0.471

Table 2
Continued

Depth CSF-A (m)	179.71	200.35	219.64	240.47	272.78	288.45	305.96	320.83	339.22	358.39
Yb	2.98	2.96	3.09	3.05	2.98	2.83	2.96	2.98	2.99	2.99
Lu	0.460	0.458	0.473	0.469	0.462	0.451	0.455	0.451	0.467	0.465
Hf	1.67	1.69	1.72	1.77	1.67	1.67	1.66	1.64	1.60	1.65
Ta	0.108	0.102	0.107	0.106	0.101	0.100	0.0972	0.0961	0.101	0.101
Th	0.115	0.111	0.108	0.112	0.110	0.100	0.0984	0.0983	0.100	0.0997
U	0.045	0.058	0.037	0.043	0.041	0.036	0.039	0.037	0.067	0.12

at ~45 m. As previously noted, Hole U1554F has high and scattered values of K_2O which may reflect mantle source enrichment and/or subsequent alteration. Second, there are small but resolvable differences between ridges and troughs—the most notable differences concern concentrations of Ti, Na and P with smaller differences in Fe, Mn and Mg. Third, major elemental concentrations are strikingly consistent with observations from the offshore and onshore segments of the Reykjanes Ridge (Figures 6a and 6j). Note that these observations exclude extremely depleted Holocene picrites.

3.2. Trace Elements

Normalized variation of average minor and trace elemental concentrations for each hole are presented in Figures 6e and 6h. There is little evidence for significant downhole variations such that the variance is generally small apart from large ion lithophiles such as Cs, Rb and Ba. Analyses from three of the four sites have patterns that are closely similar to published values for present-day submarine Reykjanes Ridge (Jones et al., 2014; Figure 6k). The obvious exception concerns analyses from Hole U1554F, which have much higher levels of enrichment, especially of the large ion lithophiles. This enrichment is strikingly similar to what has been observed for axial volcanic ridges exposed on the Reykjanes Peninsula (Peate et al., 2009).

At the less incompatible end of these diagrams, a flat stable pattern becomes emergent. Nonetheless, there are systematic differences in overall concentrations of Zr and Y so that troughs and ridges have higher and lower values of each, respectively. There is a clear positive Nb anomaly in Hole U1554F which correlates with Ti values. Finally, three sites (i.e., VST-1, VSR-1, VST-2b) have obvious Pb anomalies, which are also observed along the submarine Reykjanes Ridge.

3.3. Rare Earth Elements

Average normalized rare earth element (REE) concentrations for each hole are shown in Figures 6f and 6i. Overall, there is marked depletion of light REEs compared with heavy REEs in each case with the obvious exception of Hole U1554F. The range of observed patterns is consistent with minor and trace element measurements and it coheres with published observations from the Reykjanes Ridge (Figures 6c and 6l). Significantly, the light REE enrichment recorded for Hole U1554F closely matches the pattern of enrichment observed for the Reykjanes Peninsula. This match probably has important implications for the dynamical evolution of the Icelandic Plume.

Toward the heavy REE end, normalized concentrations are generally more uniform. Nevertheless, there are clear systematic offsets between analyses from ridges and troughs with ridges having consistently lower middle and heavy REE concentrations. There is sometimes variability at the light REE end. Note that these changes and patterns require a combination of variations in depth and degree of melting together with mantle source variation. The challenge is to tease out these different contributions using a single quantitative modeling strategy.

4. Geochemical Modeling

We wish to model major, trace and rare earth element concentrations from the drilled V-shaped ridges and troughs. Our goal is to estimate the depth and extent of melting at each site. In this way, we can calculate the cumulative amount of generated melt which in turn determines oceanic crustal thickness. Our strategy is to exploit a polybaric fractional melting description, which assumes a priori knowledge of the mantle source. This strategy

Table 3
Analyses for Hole U1563B (60°11.99462′ N, 27°59.99960′ W)

Depth CSF-A (m)	321.94	340.79	350.92	356.66	371.77	381.52	394.03	413.23	424.16	452.05
Major Elements from XRF (wt.%)										
SiO_2	50.8	50.4	51.1	51.1	49.5	52.8	52.4	53.5	50.7	51.2
TiO_2	0.93	0.94	0.87	0.88	0.81	0.84	0.82	0.82	0.95	0.95
Al_2O_3	14.2	14.1	13.8	14.0	12.9	13.7	13.4	13.5	14.2	14.1
Fe_2O_{3T}	11.4	11.8	11.2	11.6	11.6	10.8	10.7	10.8	11.8	12.0
MnO	0.18	0.17	0.17	0.18	0.17	0.17	0.16	0.16	0.18	0.18
MgO	8.81	8.78	8.76	9.02	11.4	8.95	8.92	8.93	8.42	8.57
CaO	12.0	11.9	11.7	11.8	11.3	11.7	11.4	11.5	11.8	11.9
Na_2O	1.63	1.57	1.54	1.56	1.49	1.52	1.45	1.39	1.80	1.64
K_2O	0.1	0.05	0.08	0.08	0.07	0.08	0.07	0.04	0.1	0.1
P_2O_5	0.07	0.07	0.06	0.06	0.06	0.06	0.06	0.06	0.07	0.07
LOI	0.34	0.19	0.25	−0.020	0.46	−0.090	−0.12	−0.37	0.050	−0.15
Total	100	99.8	99.4	100	99.7	101	99.2	100	100	100
Minor and Trace Elements from XRF (ppm)										
Sc	42.8	43.0	42.9	43.3	37.6	42.6	42.1	42.1	43.3	45.5
V	312	313	302	302	271	288	285	284	310	311
Cr	466	443	423	424	633	472	484	483	349	345
Ni	164	154	158	159	257	162	164	160	134	133
Cu	106	97.5	96.6	98.3	91.1	100	92.9	96.4	98.0	98.5
Zn	82.7	80.3	81.2	81.6	74.0	75.8	75.1	75.6	83.7	82.2
Sr	62.2	61.4	62.3	63.2	66.9	64.0	61.2	58.8	67.4	66.8
Y	24.5	25.2	22.8	22.6	20.4	21.7	21.5	21.3	24.3	24.0
Zr	45.8	46.4	42.7	43.0	39.5	41.9	40.8	41.0	49.3	48.8
Nb	1.4	1.4	1.4	1.5	1.1	1.1	1.1	1.1	2.1	2.1
Pb	0.4	0.4	0.7	0.6	0.7	0.6	0.4	0.6	0.7	0.5
Trace Elements from ICP-MS (ppm)										
Ga	15.1	15.6	15.0	15.7	13.2	14.2	13.9	14.1	15.8	15.1
Rb	2.50	0.689	1.58	1.52	1.55	1.42	1.29	1.06	2.16	1.88
Cs	0.073	0.015	0.024	0.015	0.061	0.034	0.032	0.011	0.043	0.042
Ba	8.90	7.67	14.4	13.9	10.6	10.8	10.3	11.4	15.0	14.4
La	1.59	1.62	1.69	1.79	1.45	1.53	1.44	1.48	2.01	2.01
Ce	4.87	5.07	5.02	5.27	4.42	4.70	4.44	4.57	5.79	5.87
Pr	0.870	0.914	0.863	0.924	0.784	0.845	0.799	0.832	0.985	0.994
Nd	5.16	5.28	4.96	5.13	4.64	4.85	4.62	4.74	5.52	5.57
Sm	2.06	2.11	1.85	1.96	1.76	1.84	1.77	1.89	2.02	2.10
Eu	0.769	0.813	0.713	0.758	0.663	0.735	0.691	0.729	0.793	0.788
Gd	2.89	2.97	2.68	2.82	2.54	2.66	2.57	2.63	2.84	2.88
Tb	0.592	0.618	0.546	0.592	0.511	0.549	0.519	0.553	0.580	0.599
Dy	4.18	4.28	3.76	4.14	3.52	3.78	3.62	3.79	4.07	4.22
Ho	0.909	0.955	0.839	0.889	0.780	0.833	0.780	0.840	0.902	0.916
Er	2.67	2.73	2.42	2.57	2.20	2.38	2.29	2.42	2.62	2.58
Tm	0.422	0.430	0.385	0.405	0.346	0.373	0.347	0.379	0.407	0.415

Table 3
Continued

Depth CSF-A (m)	321.94	340.79	350.92	356.66	371.77	381.52	394.03	413.23	424.16	452.05
Yb	2.69	2.71	2.46	2.62	2.22	2.37	2.31	2.42	2.62	2.62
Lu	0.409	0.421	0.383	0.405	0.345	0.365	0.347	0.381	0.404	0.414
Hf	1.42	1.67	1.26	1.35	1.16	1.30	1.22	1.33	1.45	1.48
Ta	0.103	0.106	0.114	0.117	0.0884	0.0951	0.0872	0.0897	0.141	0.131
Th	0.111	0.106	0.120	0.123	0.0927	0.102	0.0926	0.0919	0.141	0.144
U	0.094	0.040	0.071	0.080	0.044	0.069	0.069	0.060	0.072	0.060

contrasts with other MORB studies, which exploit individual major element proxies (e.g., $Na_{8.0}$; Gale et al., 2014). We exploit a combined forward and inverse modeling approach which is divided into four key steps. First, we tackle the central question of mantle source composition. Our approach is to construct an optimal mantle source by calibration with respect to observed crustal thickness (i.e., cumulative melt thickness) for the zero-age trough at the Reykjanes Ridge. Critically, this calibration helps to circumvent the otherwise intractable problem of not knowing the composition of the local mantle source.

Second, geochemical observations are assembled, averaged and corrected in several ways. For example, we apply a standard olivine fractionation correction to rare earth element measurements. We also use observational constraints along the Reykjanes Ridge to correct for the amount of water within the mantle source region. Third, we invert the corrected rare earth element measurements using a polybaric melting model within which predetermined, but testable, parameter assumptions are embedded. Finally, the recovered melt fraction as a function of depth is used to forward model major and trace element concentrations. This forward modeling is an important sense check and in this way we embrace major, minor, trace and rare earth element observations within a unified model. We recognize that these geochemical data can be modeled in other ways and we acknowledge that the results presented in this contribution are just a first tentative step.

4.1. Mantle Sources

In the past, it was generally agreed that the mantle source region within the vicinity of the Icelandic Plume comprises at least two significant components—a Primitive Mantle (PM) source component, which probably upwells through a putative plume conduit from deep within the mantle, and a Depleted Mantle (DM) source component (Figure 7a). This historical consensus was primarily based upon detailed geochemical studies of dredged basaltic glasses along the Reykjanes Ridge (Blichert-Toft et al., 2005; Murton et al., 2002; Schilling, 1973). One way of presenting this information is to examine ϵ_{Nd} values as a function of distance from the center of the Icelandic Plume (Figure 7b). These values vary between 5 and 10 over a radial distance of 1500 km. $\epsilon_{Nd} = 10$ and lower values (i.e. $\epsilon_{Nd} < 5$) are thought to be indicative of Depleted Mantle and Primitive Mantle, respectively (McDonough & Sun, 1995). Since the long wavelength variation of ϵ_{Nd} is smooth and systematic, it has been argued that efficient binary mixing occurs along the Reykjanes Ridge (Schilling, 1973). Notwithstanding this elegant argument, geochemical measurements from Iceland itself indicate that binary mixing of PM and DM constrained by Nd isotopic variation is undoubtedly an oversimplification and we acknowledge that additional source components such as garnet pyroxenite, which may be derived from subducted oceanic crust, exist and play an additional role (Shorttle et al., 2014; Willbold & Stracke, 2006).

Here, our strategy is to start with the simplest possible source that is consistent with independent observations. Critically, it is generally recognized that the mantle source becomes increasingly depleted along the Reykjanes Ridge such that by 60°N, the source region primarily comprises uniform depleted mantle (Kempton et al., 2000; Shorttle & Maclennan, 2011). The consequences of assuming more sophisticated mantle source compositions can be explored as dictated by the results of this initial inverse and forward modeling. Our starting assumption is that source composition along the Reykjanes Ridge is determinable by binary mixing between, say, PM and DM end-members where PM has the same composition as Bulk Silicate Earth, which is defined by McDonough and Sun (1995) as "pyrolite" or "the pyrolite model" (see their Table 5). Composition of the DM end member is less precisely known. Depletion of the upper mantle is often calculated by extracting enriched continental crust from, say, 40% of the mantle (O'Nions et al., 1979). Part of this depletion may arise from sequestering of subducted

Table 4
Analyses for Hole U1554F (60°07.51360′ N, 26°42.11400′ W)

Depth CSF-A (m)	649.77	664.43	681.88	699.58	710.95	719.20	737.36	749.96	761.95	778.57
Major Elements from XRF (wt.%)										
SiO_2	47.6	48.7	48.2	48.3	48.3	47.2	47.7	47.8	48.0	47.4
TiO_2	1.6	1.6	1.6	1.7	1.6	1.6	1.6	1.6	1.6	1.6
Al_2O_3	14.2	13.7	13.5	13.9	13.7	13.8	13.8	13.8	14.0	13.8
Fe_2O_{3T}	13.4	13.4	13.5	13.5	13.4	13.5	13.5	13.5	12.4	13.1
MnO	0.19	0.19	0.19	0.19	0.19	0.20	0.20	0.19	0.18	0.19
MgO	7.59	7.92	8.09	7.73	7.78	8.05	8.21	7.92	7.28	7.31
CaO	11.8	11.8	11.4	11.9	11.7	12.1	11.8	11.8	11.9	11.7
Na_2O	1.79	1.74	1.71	1.77	1.76	1.73	1.78	1.72	1.81	1.77
K_2O	0.2	0.3	0.4	0.09	0.4	0.3	0.3	0.2	0.3	0.5
P_2O_5	0.2	0.2	0.2	0.2	0.2	0.2	0.2	0.2	0.2	0.2
LOI	1.3	1.2	0.93	0.69	1.1	1.2	0.97	0.96	2.3	2.1
Total	99.7	101	99.5	99.8	100	99.9	100	99.6	99.9	99.5
Minor and Trace Elements from XRF (ppm)										
Sc	43.9	39.7	40.0	39.0	41.8	41.3	41.9	41.0	42.2	42.8
V	342	316	314	314	323	324	321	321	328	328
Cr	369	346	355	324	358	357	361	362	369	366
Ni	133	134	135	115	127	134	139	134	148	137
Cu	156	148	149	146	150	147	150	143	155	152
Zn	109	98.5	101	95.8	101	103	101	102	106	105
Sr	132	150	135	136	138	135	135	133	136	133
Y	29.1	28.6	27.6	28.8	28.4	28.3	28.6	28.2	28.7	28.7
Zr	85.0	84.5	82.2	84.0	84.1	83.5	83.8	83.7	84.1	83.9
Nb	10	10	9.8	9.9	9.8	9.8	10	9.7	9.8	9.8
Pb	0.7	0.7	0.7	0.5	0.8	0.4	0.7	1	0.9	2
Trace Elements from ICP-MS (ppm)										
Ga	17.0	16.9	16.6	16.5	16.7	16.8	15.9	16.7	18.0	17.7
Rb	2.44	4.32	8.40	1.18	8.38	5.64	6.01	3.94	6.15	12.8
Cs	0.046	0.14	0.35	0.033	0.41	0.16	0.27	0.084	0.27	0.44
Ba	26.3	43.3	44.6	36.0	52.4	31.6	37.1	49.3	41.8	27.9
La	6.72	6.74	6.56	6.48	6.68	6.57	6.54	6.81	6.74	6.68
Ce	16.9	16.9	16.4	16.1	16.8	16.7	16.5	17.2	17.1	16.8
Pr	2.54	2.55	2.45	2.42	2.46	2.49	2.48	2.52	2.54	2.54
Nd	12.4	12.5	11.8	11.9	12.1	12.3	12.1	12.4	12.4	12.4
Sm	3.67	3.54	3.40	3.44	3.50	3.61	3.55	3.65	3.66	3.55
Eu	1.30	1.31	1.27	1.24	1.30	1.32	1.30	1.32	1.32	1.26
Gd	4.39	4.34	4.24	4.32	4.34	4.42	4.32	4.42	4.39	4.39
Tb	0.818	0.804	0.782	0.776	0.797	0.791	0.801	0.804	0.829	0.803
Dy	5.25	5.32	5.07	5.20	5.17	5.27	5.21	5.21	5.31	5.16
Ho	1.09	1.12	1.06	1.08	1.08	1.09	1.08	1.11	1.11	1.09
Er	3.08	3.07	2.94	3.04	3.00	3.01	3.02	3.08	3.10	3.07
Tm	0.455	0.469	0.453	0.465	0.466	0.447	0.456	0.454	0.472	0.470

Table 4
Continued

Depth CSF-A (m)	649.77	664.43	681.88	699.58	710.95	719.20	737.36	749.96	761.95	778.57
Yb	2.90	2.89	2.80	2.83	2.83	2.84	2.81	2.90	2.94	2.92
Lu	0.435	0.428	0.417	0.432	0.433	0.424	0.430	0.447	0.445	0.438
Hf	2.36	2.37	2.29	2.31	2.30	2.36	2.29	2.40	2.42	2.35
Ta	0.655	0.647	0.620	0.642	0.632	0.634	0.647	0.655	0.650	0.653
Th	0.414	0.411	0.394	0.393	0.402	0.401	0.404	0.424	0.416	0.404
U	0.13	0.14	0.17	0.14	0.16	0.14	0.19	0.14	0.20	0.21

oceanic crust deep within the mantle. An alterative approach measures the composition of abyssal peridotites that represent the residue of partial melting at mid-oceanic ridges (Workman & Hart, 2005). Finally, Salters and Stracke (2004) determined the average composition of depleted mantle by adopting a combination of observational and modeling approaches.

Binary mixing along the Reykjanes Ridge between PM and DM can be represented by a concentration, C, which varies between these two end-members as a function of time and space. The behavior of C is modeled using a partial differential equation which assumes that C is a function of one spatial dimension, x, and time, t. Thus

$$\frac{\partial C}{\partial t} = -v\frac{\partial C}{\partial x} - \lambda C \tag{1}$$

where v is the velocity in the positive x direction at which C horizontally advects and λ determines the decay rate. Here, we assume that v is constant but similar results are obtained if v varies as a function of x. This equation shows that the local rate of change of concentration based upon the amount of PM balances advection by the prevailing flow and decay caused by plate spreading. At steady state, it reduces to

$$v\frac{\mathrm{d}C}{\mathrm{d}x} = -\lambda C \tag{2}$$

For binary mixing between PM and DM, the solution to this equation is given by

$$C = C_{PM}\exp(-x/\tau v) + C_{DM}(1 - \exp(-x/\tau v)) \tag{3}$$

where $\tau = 1/\lambda$ is the characteristic decay time which is controlled by plate spreading in this case.

Values of C_{PM} and C_{DM} are chosen to be $\epsilon_{\mathrm{Nd}} = 5$ (i.e., not purely PM) and $\epsilon_{\mathrm{Nd}} = 10$, respectively. Using these end-member values, we calculate the mantle source composition at any position along the Reykjanes Ridge. If the horizontal flow within the plume is $v = 200$ km/Myrs and if $\tau v = 300$ km, which is the distance over which C decreases by $1/e$ then $\tau = 1.5$ Myrs. In this way, we can match ϵ_{Nd} values along the ridge axis (Figure 7b). Since the value of v is determined by plume flux, binary mixing between PM and DM therefore represents an independent method for estimating plume flux which can be corroborated by other observations such as plume planform (Parnell-Turner et al., 2014). Horizontal flow within the plume head is obtained from the propagation velocity of each VSR, which is determined by the angle between any given VSR and the MOR (Figure 2). It is evident, by inspection, that VSR-3 yields a faster propagation velocity compared with VSR-1 and VSR-2 (i.e., 400 km/Myrs and 200 km/Myrs, respectively). This difference can account for the fact that, at VSR-3, $\epsilon_{\mathrm{Nd}} = 7.81$ because a larger value of v carries plume material with low values of ϵ_{Nd} further along the MOR (Figure 7). These results imply that variable buoyancy flux of the Icelandic Plume may play an important role in changing mantle source composition as material flows away from Iceland (Poore et al., 2009).

Table 5
Analyses for Hole U1562B (60°06.29930′ N, 26°30.10260′ W)

Depth CSF-A (m)	432.39	442.43	453.63	466.75	482.62	495.55	508.43	523.18	542.97	557.82
Major Elements from XRF (wt.%)										
SiO_2	49.7	53.3	53.7	50.6	50.8	52.0	52.2	51.8	52.7	49.8
TiO_2	0.84	0.79	0.77	0.83	0.70	0.75	0.75	0.81	0.73	0.77
Al_2O_3	14.4	13.5	13.6	14.3	14.9	13.4	13.5	13.6	13.2	14.0
Fe_2O_{3T}	10.9	10.3	10.3	10.9	9.96	10.3	10.3	10.8	10.3	10.7
MnO	0.16	0.16	0.16	0.17	0.15	0.16	0.16	0.17	0.16	0.16
MgO	9.61	9.17	9.02	9.72	9.19	8.78	9.00	9.28	9.25	9.26
CaO	11.9	11.4	11.3	12.1	12.9	12.0	11.9	11.9	11.5	12.4
Na_2O	1.59	1.36	1.42	1.46	1.43	1.40	1.36	1.39	1.72	1.50
K_2O	0.06	0.05	0.05	0.05	0.1	0.1	0.1	0.07	0.09	0.1
P_2O_5	0.06	0.05	0.05	0.06	0.05	0.06	0.06	0.06	0.06	0.06
LOI	0.49	−0.20	−0.40	−0.35	0.47	0.36	0.90	−0.20	−0.26	0.60
Total	99.7	99.9	99.9	99.9	101	99.2	100	99.8	99.5	99.4
Minor and Trace Elements from XRF (ppm)										
Sc	40.3	38.4	39.3	41.9	44.4	42.3	43.3	42.7	41.9	44.3
V	276	264	260	276	285	281	284	291	283	303
Cr	470	478	475	506	493	469	476	514	540	560
Ni	190	190	182	195	182	162	182	175	191	193
Cu	98.5	94.5	94.1	99.3	123	99.5	95.4	103	99.7	104
Zn	73.6	71.6	70.4	74.9	73.5	76.3	78.7	78.5	74.5	79.3
Sr	81.9	74.7	74.1	79.0	68.3	66.0	65.4	62.7	60.9	67.9
Y	19.6	18.9	18.1	19.8	17.2	19.4	19.2	19.6	18.6	19.5
Zr	36.7	34.5	34.0	36.6	32.3	35.7	35.4	37.2	33.9	36.6
Nb	1.1	0.82	0.96	1.0	1.1	1.3	1.3	1.1	1.1	1.1
Pb	0.3	0.4	0.8	0.5	0.3	0.7	0.5	0.9	0.5	0.5
Trace Elements from ICP-MS (ppm)										
Ga	14.2	13.2	13.0	13.5	13.4	12.9	13.1	13.9	12.5	13.4
Rb	1.06	1.13	1.05	1.06	1.8	2.08	2.33	1.23	1.50	2.78
Cs	0.020	0.014	0.017	0.010	0.029	0.045	0.049	0.016	0.020	0.085
Ba	11.3	12.4	11.7	11.2	7.11	14.7	13.7	13.8	16.6	7.43
La	1.51	1.45	1.38	1.43	1.65	1.65	1.66	1.61	1.65	1.56
Ce	4.58	4.31	4.10	4.30	4.64	4.61	4.71	4.72	4.58	4.46
Pr	0.809	0.752	0.730	0.771	0.769	0.773	0.771	0.801	0.759	0.799
Nd	4.80	4.30	4.17	4.37	4.24	4.32	4.33	4.48	4.24	4.38
Sm	1.75	1.66	1.61	1.83	1.54	1.62	1.60	1.69	1.58	1.64
Eu	0.727	0.653	0.640	0.677	0.613	0.618	0.634	0.688	0.616	0.643
Gd	2.56	2.30	2.26	2.41	2.11	2.27	2.27	2.39	2.22	2.38
Tb	0.505	0.476	0.457	0.486	0.432	0.468	0.468	0.483	0.458	0.486
Dy	3.61	3.24	3.13	3.34	3.10	3.23	3.22	3.49	3.19	3.34
Ho	0.760	0.702	0.695	0.726	0.663	0.705	0.723	0.762	0.694	0.708
Er	2.19	2.03	1.91	2.10	1.94	2.09	2.06	2.16	2.03	2.09
Tm	0.350	0.329	0.309	0.316	0.311	0.323	0.334	0.343	0.316	0.328

Table 5
Continued

Depth CSF-A (m)	432.39	442.43	453.63	466.75	482.62	495.55	508.43	523.18	542.97	557.82
Yb	2.21	1.96	1.92	2.06	1.97	2.09	2.05	2.15	2.08	2.08
Lu	0.332	0.298	0.296	0.320	0.303	0.321	0.321	0.327	0.313	0.325
Hf	1.19	1.08	1.03	1.10	0.979	1.09	1.04	1.15	1.04	1.10
Ta	0.0978	0.0843	0.0841	0.0878	0.113	0.115	0.114	0.103	0.115	0.102
Th	0.0998	0.103	0.0920	0.0927	0.131	0.128	0.127	0.110	0.124	0.111
U	0.040	0.046	0.055	0.035	0.11	0.075	0.054	0.056	0.049	0.14

4.2. Data Preparation and Model Assumptions

Major element, trace element and REE concentrations are assembled and corrected in the following way. The two most important corrections addressed here concern olivine fractionation of the samples and water content of the mantle source.

If mid-oceanic ridge basalts are sufficiently primitive and have undergone principally olivine fractionation, major element compositions of primary melts can be inferred by incrementally adding back olivine. Under the assumption that no REEs are present in cumulate olivines, REE concentrations of the primary melt can be calculated from measured REE concentrations. It is possible to check for chemical equilibrium between a modeled basaltic liquid and its mantle source by exploiting the exchange of Fe and Mg between melt and olivine. In particular, the calculated forsterite content of olivine in equilibrium with the melt should be the same as that of the inferred mantle source. Three parameters are required in order to calculate the equilibrium Fo number of primordial olivine, whose value determines whether or not a correction for olivine fractionation is required.

First, the value of the olivine/melt distribution coefficient, KD (Fe/Mg), is required. Here, we use KD (Fe/Mg) = 0.3 (Roeder & Emslie, 1970). We then need to know the Fo number of olivine within the source, which is assumed to be 90 (Lee et al., 2009). Finally, since the Fo number considers only Fe^{2+} rather than Fe^{3+}, the $Fe^{3+}/\sum Fe$ ratio is required. A constant value of $Fe^{3+}/\sum Fe = 0.1$ is generally regarded as appropriate for mid-oceanic ridges (Brounce et al., 2014; Cottrell & Kelley, 2011). Here, we use the measurements carried out by Shorttle et al. (2015) where $Fe^{3+}/\sum Fe = 0.147$ for the zero-aged trough and $Fe^{3+}/\sum Fe = 0.144$ for the zero-age ridge. These values fractionally reduce the amount of olivine, that is, added back, yielding slightly more elevated corrected REE concentrations. It is important to emphasize that uncertainties in $Fe^{3+}/\sum Fe$ do not significantly affect our results.

This method was used to calculate the forsterite content of olivines in equilibrium with basaltic liquid with the same array of compositions as the measured whole-rock samples. When this value is less than 90, an olivine correction must be applied whereby SiO_2, FeO, and MgO are progressively added to the composition of the whole rock until the olivine which is in equilibrium with the rock reaches an Fo of 90. For example, whole-rock samples analyzed from Hole U1562B have olivine Fo numbers of 86.9–87.7. In order to obtain an olivine Fo value of 90, 8.4–10.6 wt.% of olivine must be added back. Consequently, the wt.% values of SiO_2, FeO and MgO change while the wt.% values of all other elements are diluted by a factor of 100/(100 + ol wt.%). This calculation works well for trace and rare earth elements but it is more problematic for Cr and Ni. A detailed description of these olivine back-calculations are given by Tatsumi et al. (1983).

H_2O content of the mantle source region is calculated using a well-known empirical relation based upon analysis of MORB and plume-influenced samples (Dixon et al., 2002; Michael, 1995). Our starting point is a densely sampled suite of H_2O measurements from basalt glass samples assembled by Nichols et al. (2002). At the zero-age trough, H_2O concentration in glass is 0.207 wt.% for MgO values of 8 wt.%. At this location, Ce in glass is 5.97 ppm, which yields a H_2O/Ce value of 342. At the zero-age ridge, H_2O in glass is 0.172 wt.% for MgO values of 8 wt.%. At this location, Ce in glass is 4.64 ppm which yields a H_2O/Ce value of 371. For the revised calibrated mantle source, these values are used to calculate source water contents of 148 and 161 ppm, respectively. This 13 ppm difference in H_2O values between trough and ridge is modest and does not materially affect our modeling results.

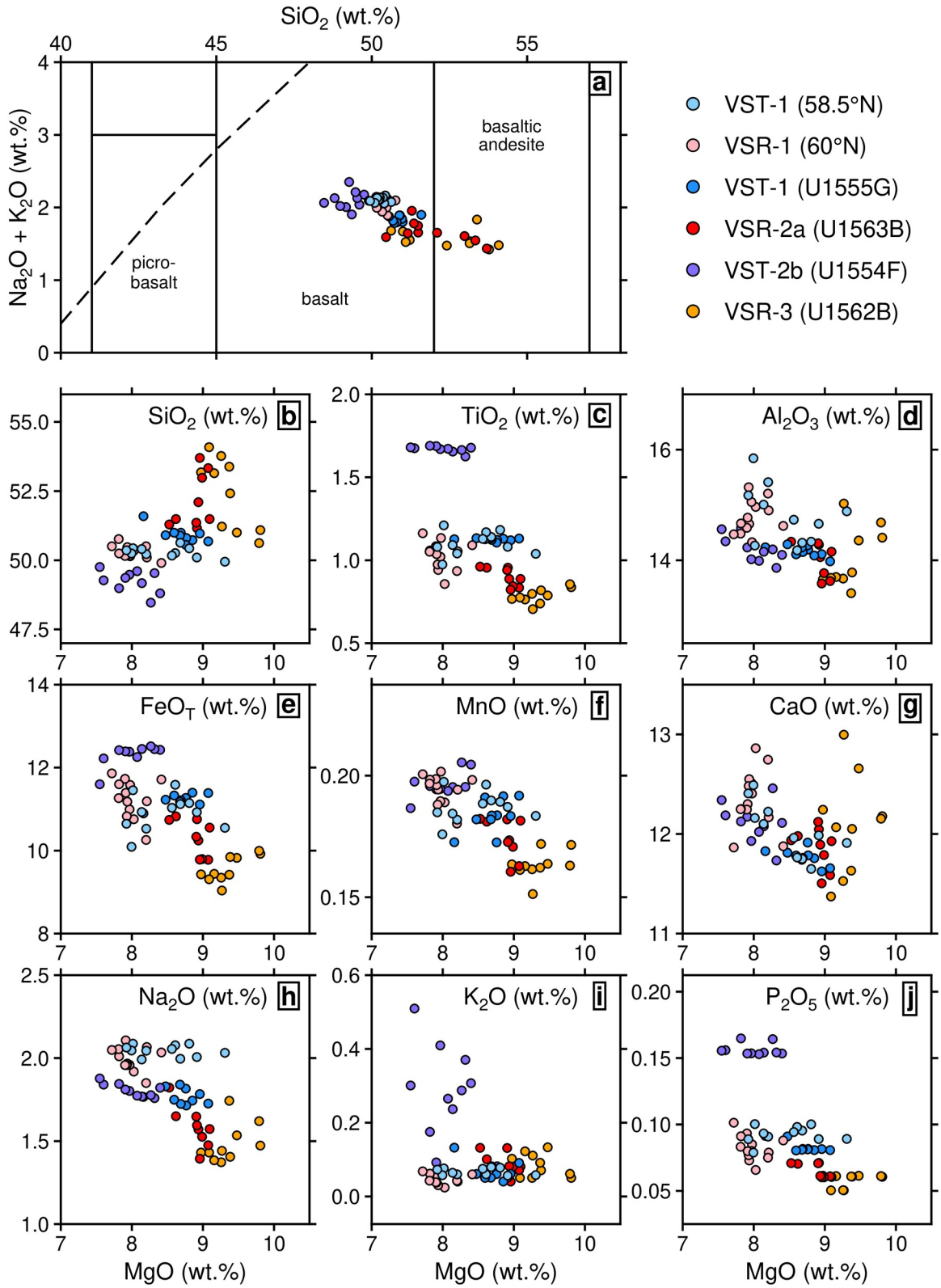

Figure 5. TAS Plot and Variation Diagrams. (a) Total Alkalis (i.e., $Na_2O + K_2O$) plotted as function of SiO_2. Solid black lines = general classification of volcanic rocks (Le Maitre, 1989); dashed line = dividing line between alkaline and sub-alkaline rocks (Irvine & Baragar, 1971); circles = individual whole-rock analyses colored as in Figure 1 (see key). (b) SiO_2 plotted as function of MgO. (c–j) Other major element oxides plotted as functions of MgO.

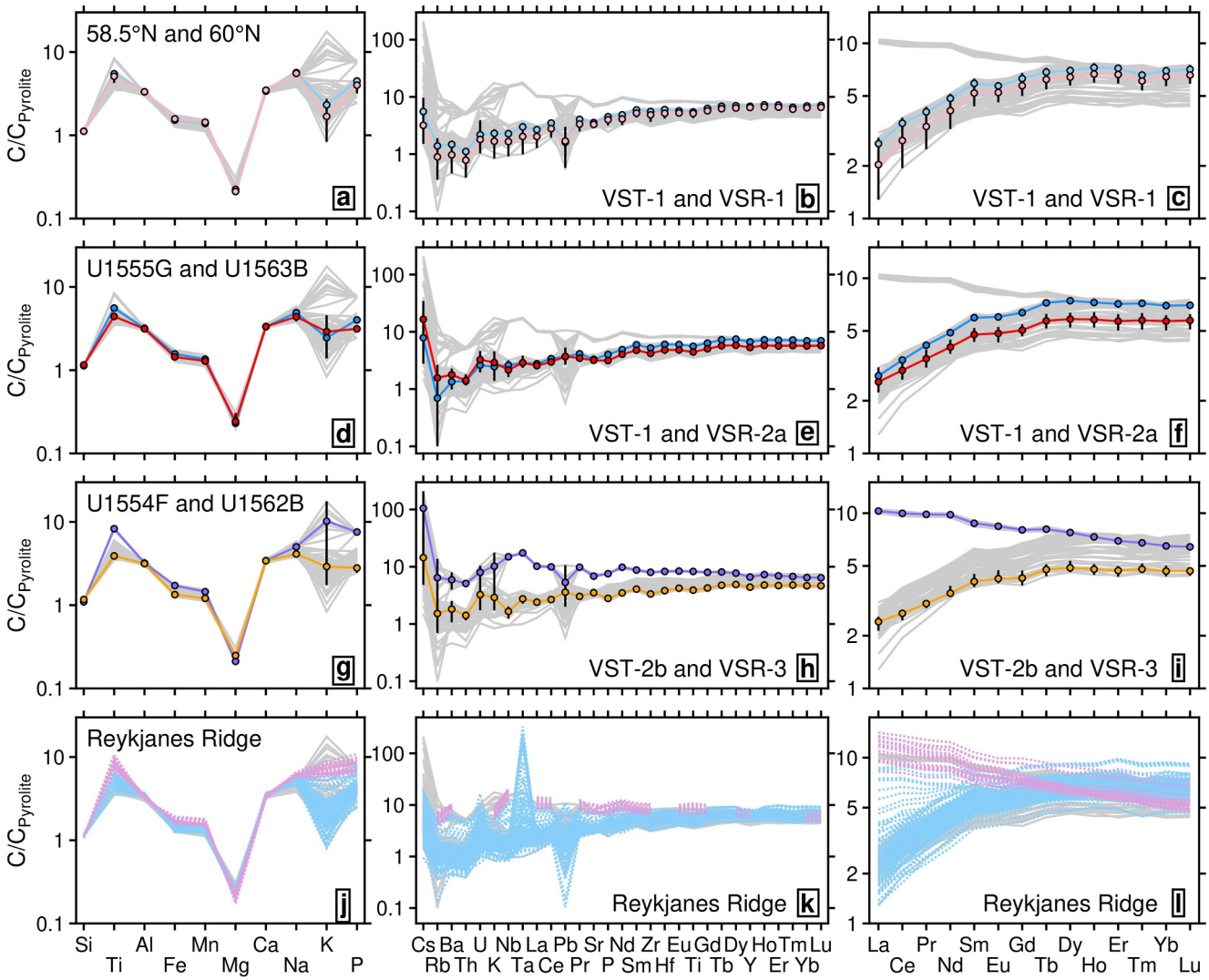

Figure 6. Summary of Geochemical Analyses. (a) Legacy major element analyses of dredged glass and whole-rock samples from specific loci along zero-age Reykjanes Ridge shown on Figure 2 (Jones et al., 2014; Murton et al., 2002). Turquoise/pink circles with vertical black lines = averaged concentrations at given V-shaped trough/ridge loci normalized with respect to the specific pyrolite model for Primitive Mantle (PM) defined by McDonough and Sun (1995); gray lines = analyses from panels (d, g). (b) Same for legacy minor and trace element analyses. Gray lines = analyses from panels (e, h). (c) Same for legacy rare earth element analyses. Gray lines = analyses from panels (f, i). (d) Major element analyses of drilled whole-rock samples from sites U1555G and U1563B. (e) Minor and trace element analyses from sites U1555G and U1563B. (f) Rare earth element analyses from sites U1555G and U1563B. (g–i) Same for sites U1554F and U1562B. (j) Legacy major element analyses of glass and whole-rock samples from Reykjanes Ridge and Reykjanes Peninsula. Turquoise dotted lines = legacy analyses for dredged samples located between 55.5°N and 63°N (Jones et al., 2014; Murton et al., 2002); plum dotted lines = legacy analyses for field samples from axial volcanic ridges exposed on Reykjanes Peninsula (Peate et al., 2009). (k) Same for legacy minor and trace element analyses. (l) Same for legacy rare earth element analyses.

Corrected major, trace and rare earth element concentrations are averaged and normalized so that geochemical modeling can be carried out. Here, we use the INVMEL-v12 software package originally developed by McKenzie and O'Nions (1991) to calculate the depth and degree of mantle melting from the compositions of different igneous rocks (see Ball et al. (2021) for revised implementation). During inverse modeling, the misfit between observed and calculated concentrations of REEs is minimized by systematically varying melt fraction as a function of depth. In this polybaric scheme, REE concentrations are calculated by integrating instantaneous melt compositions along different isentropic melting paths. The relationship between melt fraction and temperature is calculated using the revised equations of Katz et al. (2003) for a suitable range of H_2O concentrations with the slightly modified parameterization described by Shorttle et al. (2014).

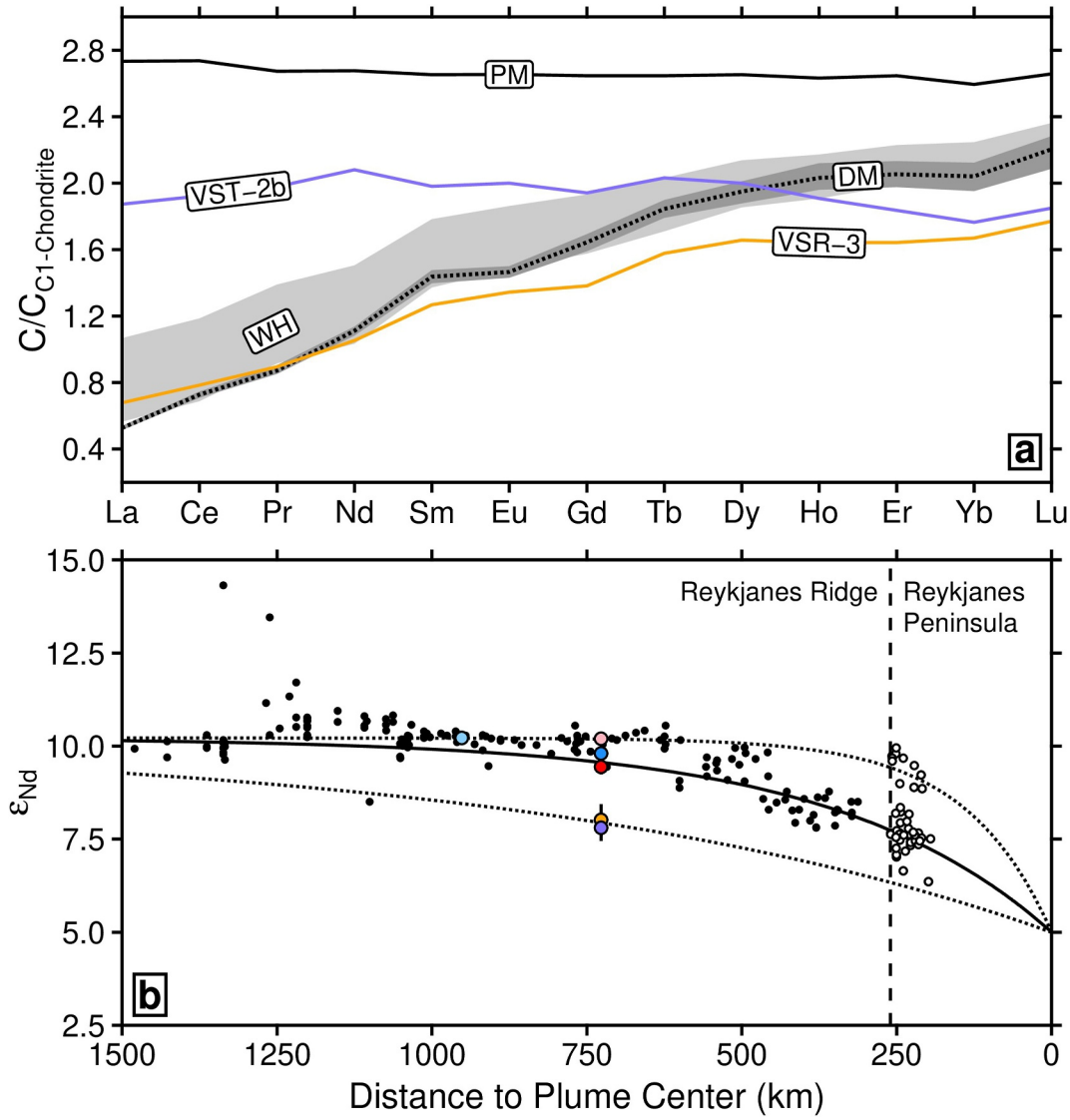

Figure 7. Mantle Source Rock Compositions. (a) Concentrations of rare earth elements normalized with respect to C1-Chondrite for different mantle source compositions. This normalization is used for clarity. Black line labeled "PM" = Primitive Mantle (McDonough & Sun, 1995); dotted line with dark gray band labeled "DM" = Depleted Mantle composition and its uncertainty used in this study and obtained by calibrated modeling of rare earth element concentrations for zero-age trough (see Figures 8a and 8b); light gray band labeled "WH" = range of depleted mantle compositions calculated by Workman and Hart (2005) where position of label indicates locus of their average composition; purple line labeled "VST-2b" = mantle source composition obtained by calibrated modeling of rare earth element concentrations for old trough VST-2b (see Figures 9e and 9f); orange line labeled "VSR-3" = mantle source composition obtained by calibrated modeling of rare earth element concentrations for old ridge VSR-3 (see Figures 9e and 9f). (b) Observed and calculated values of ϵ_{Nd} plotted as function of distance from center of Icelandic Plume. Solid black circles = offshore measurements assembled by Blichert-Toft et al. (2005), by Murton et al. (2002), by Thirlwall et al. (2004), and by Jones et al. (2014); open circles = onshore measurements from Thirlwall et al. (2004), Kokfelt et al. (2006), and Peate et al. (2009); blue/red and purple/orange circles with vertical lines = measured values of ϵ_{Nd} for young and old trough-ridge pairs (Pearman et al., 2026); solid/dotted curves = relationship between ϵ_{Nd} and runout distance, which depends upon plume flux (see text for further details); vertical dashed line = Icelandic coastline.

In order to implement the INVMEL-v12 package, the values of three sets of input parameters are fixed in advance, although it is important to emphasize that changing these values within appropriate bounds can, and should, be carefully tested which is what we have done here. First, REE concentrations within the mantle source, which are calculated from binary (or ternary) mixing of different end-members whose proportions are often, but

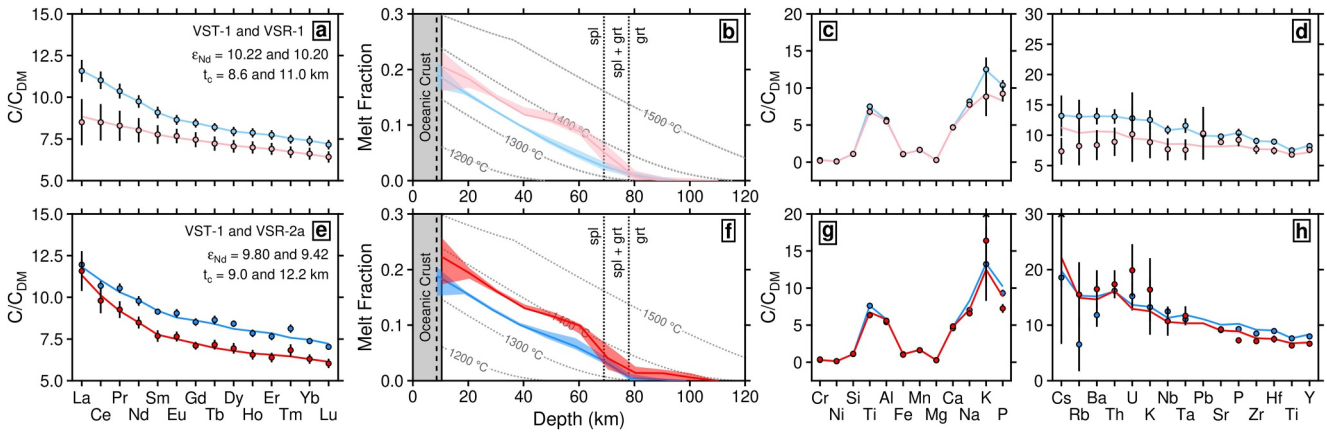

Figure 8. Geochemical Modeling of Zero-Age and Young VSTs and VSRs. (a) Observed and calculated concentrations of rare earth elements normalized with respect to our calculated Depleted Mantle (DM) composition (see Figure 7a). Turquoise/pink circles with vertical bars = average concentrations $\pm 1\sigma$ corrected for olivine fractionation at zero-age ST-1 and zero-age VSR-1, respectively (Jones et al., 2014); turquoise/pink lines = best-fitting concentrations calculated by inverse modeling using melt fraction distribution as function of depth shown in panel (b). Values of ϵ_{Nd} and of t_c = 8.6 km for trough are taken from Jones et al. (2014) and from Poore et al. (2011), respectively. (b) Turquoise/pink lines with bands = optimal melt fractions as function of depth for zero-age VST-1 and zero-age VSR-1 obtained by minimizing misfit between observed and calculated rare earth element concentrations shown in panel (a) where width of each band represents uncertainty obtained by *Monte Carlo* modeling with 1000 iterations; gray dotted lines with temperature labels = melt fractions as function of depth and temperature calculated exploiting approach described by McKenzie (1984) and by Katz et al. (2003) with revised parameters from Shorttle et al. (2014); vertical dotted lines = garnet-spinel transition (69–78 km) taken from Tomlinson and Holland (2021); gray rectangle along left-hand side = observed thicknesses of oceanic crust whose bases represent top of melting column where solid/dashed lines are bases of crust for VST-1 (8.6 km) and VSR-1 (10.4 km), respectively (Poore et al., 2011). (c, d) Observed and calculated concentrations of other major, minor and trace elements where calculated concentrations are obtained by forward modeling using melt fractions as function of depth recovered by inverting rare earth element concentrations. (e–h) Same for young VST-1 and young VSR-2a. Values of ϵ_{Nd} are taken from Pearman et al. (2026).

not always, determined using measured values of ϵ_{Nd}. Second, the partition coefficients of REEs between solid and melt phases, which have been calculated using the lattice strain parameterization of Blundy and Wood (2003). A useful summary of these values is provided by Gibson and Geist (2010). Finally, the depth and thickness of the spinel-garnet phase transition zone, which determines the aluminous phases that are present within the mantle source. Here, we adopt a depth range of 69–78 km in accordance with the thermodynamical modeling of Tomlinson and Holland (2021).

4.3. Zero-Age Ridge-Trough Pair

We start by building models for the zero-age ridge-trough pair using an approach originally described by Poore et al. (2011). The reason for revisiting the actively forming pair is threefold. First, detailed dredging expeditions have yielded a densely sampled suite of fresh basaltic glasses and rocks which, with the aid of modeling, should provide important insights into the general mechanism by which V-shaped ridges and troughs form. Second, by examining zero-age observations in conjunction with pairs of young and old ridges and troughs, we can potentially unlock a valuable temporal sequence of plume behavior over a complete 14 Ma period. Third, independent crustal thickness constraints are available at the MOR, which help to constrain the relationship between melt generation and mantle source.

We first model the zero-age trough where oceanic crustal thickness is 8.6 ± 0.5 km (Figure 2; Smallwood et al., 1995). At this location, ϵ_{Nd} = 10.22, which indicates that the mantle source is dominated by the DM end-member (Figure 7b). If we reasonably assume that melt fraction as a function of depth has a fixed isentropic temperature of 1350°C during decompression and that the integrated melt thickness equates to 8.6 km, we can constrain the mantle source composition, which is consistent with the results of Workman and Hart (2005) shown in Figure 7a. Observed and calculated REE concentrations agree and the forward-modeled concentrations of major, minor and trace elements generally match observations (Figure 8). Note that the quoted uncertainty in crustal thickness only has a minor effect upon this mantle source calculation.

We can now address the adjacent zero-age ridge which is located further north (Figure 2). At this location, ϵ_{Nd} = 10.20, which suggests that the mantle source is essentially unchanged (Murton et al., 2002). Normalized concentrations of REEs are slightly lower than at the trough (Figure 8a). Inverse modeling was carried out to

calculate the optimal melt fraction as a function of depth that minimizes the misfit between observed and predicted REEs. Once again, the agreement between observed and calculated major elements, trace elements and REEs is excellent. Our results show that melt fraction as a function of depth is consistent with an average mantle temperature of ~1380°C (i.e., 25–30°C hotter; Figure 8b). A significant feature of this melt profile is suppression of isentropic melting at depths greater than ~65 km, which is consistent with the results reported by Poore et al. (2011). There is also some evidence for slightly elevated temperatures within the lower half of the melting column between 40 and 60 km.

A central concern is whether or not the differences between these two melting profiles are resolvable given observational uncertainties. We can address this concern in two ways. First, it is evident that the average REE concentrations at each location are different: The variance is small, especially for heavy REEs, with the largest variance for light REEs from the V-shaped ridge. Second, we have used *Monte Carlo* simulations to characterize the uncertainties associated with the two recovered melting profiles (Figure 8b; Press et al., 1988). Random noise was added to REE concentrations to generate 1000 synthetic data sets which were then individually inverted. In this way, observational uncertainty is mapped into the model space, which shows that two melting profiles are resolvably different to each other. In summary, these melting profiles are offset from each other, which is indicative of a difference in source temperature and in the case of the V-shaped ridge, the base of the melting profile appears to be slightly suppressed (i.e., cooler).

4.4. Young (2.8–5.2 Ma) Ridge-Trough Pair

We now turn our attention to holes U1555G and U1563B, which are representative of VST-1 and VSR-2a (Figures 8e–8h). Thus the young trough and the zero-age trough are the same since they are manifestations of a single continuous diachronous feature. We first model the young trough where oceanic crustal thickness is reasonably assumed to be similar to that of the zero-age trough (i.e., 8.1–9.1 km; Smallwood et al., 1995). At this location, $\epsilon_{Nd} = 9.80$ which suggests that the mantle source is not quite as depleted as before. We use the well-known binary mixing relationship to calculate the source composition by mixing PM and DM (McKenzie & O'Nions, 1991). *Monte Carlo* inverse modeling yields a good fit between observed and calculate REE concentrations for a melt fraction as a function of depth that is consistent with an isentropic temperature of 1350°C (Figure 8f). Cumulative melt thickness is 9.1 km and the forward-modeled concentrations of most major, minor and trace elements agree with observation with the exception of the large-ion lithophiles. Significantly, we obtain a similar result if the trace element composition of the enriched component of the source is determined from a mixture of DM and recycled MORB (Pearman et al., 2026; Shorttle et al., 2014). Crucially, an inverse modeling approach can be used to assess the role of changing the trace element composition of the assumed source.

We address the young ridge in a similar way. Here, $\epsilon_{Nd} = 9.42$, which indicates that the mantle source could be slightly more isotopically enriched compared with rocks from the young trough. This modest enrichment is manifest at the light REE end where ridge and trough concentrations converge. Once again, *Monte Carlo* inverse modeling yields a good fit between observed and calculated REE concentrations. Major, minor and trace element concentrations are accurately matched. Significantly, the calculated melt fraction as a function of depth is closely similar to that obtained for the zero-age ridge with an average mantle temperature of ~1380°C. As before, melting is suppressed at depth, which is indicative of a cooler base (Poore et al., 2011). The cumulative melt thickness is 12.2 km, which is consistent with the calculated residual depth anomaly Parnell-Turner et al. (2014). Once again, inclusion of a minor pyroxenite component yields an almost identical result (Pearman et al., 2026; Shorttle et al., 2014).

4.5. Old (12.7–13.9 Ma) Ridge-Trough Pair

Finally, we consider holes U1554F and U1562B, which sample VST-2b and VSR-3 (Figure 9). As before, we start by modeling the old trough where there are no crustal thickness measurements although an estimate of the residual depth anomaly suggests that crustal thickness variation is probably similar to that found beneath the young and zero-age troughs. At this location, $\epsilon_{Nd} = 7.81$, which is indicative of a mantle source, that is, significantly more enriched than at the younger sites (Pearman et al., 2026). This enrichment is manifest by unusually elevated concentrations of light REEs (Figure 9a).

In order to investigate the relationships and potential trade-offs between mantle source composition and melt profile, we present the results of three different *Monte Carlo* inverse models. Discussion of these three models is

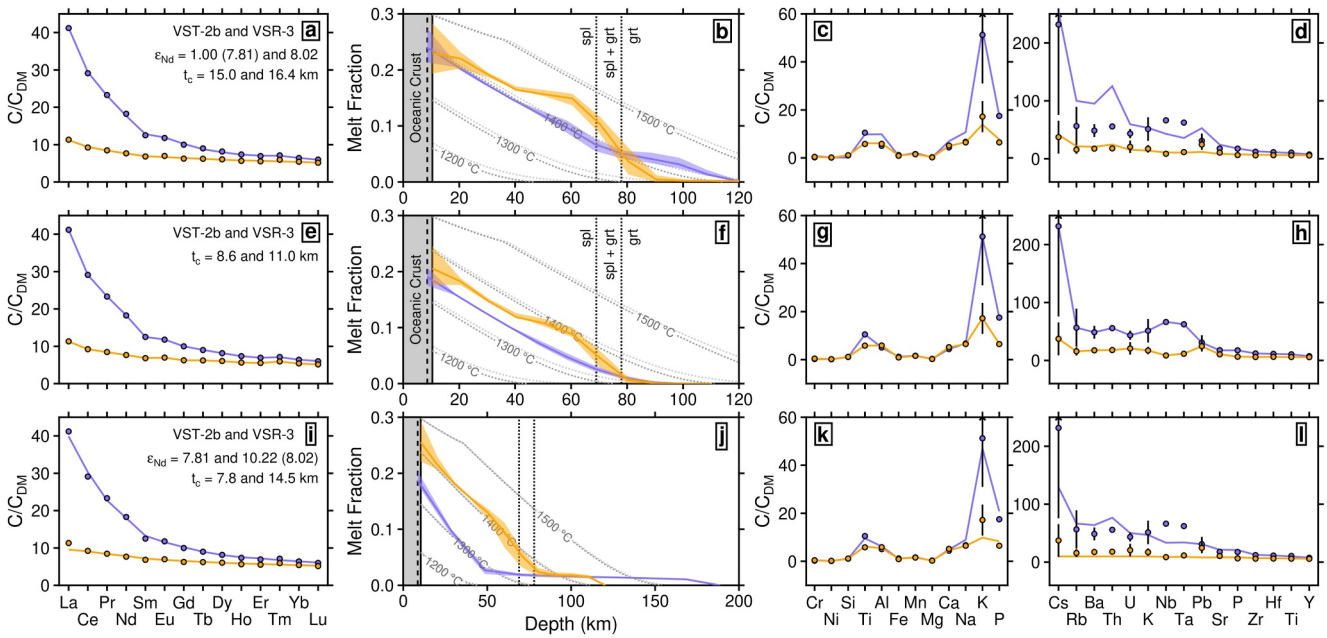

Figure 9. Geochemical Modeling of Old VST and VSR. (a) Observed and calculated concentrations of rare earth elements normalized with respect to our calculated Depleted Mantle (DM) composition (see Figure 7a). Purple/orange circles with vertical bars = average concentrations corrected for olivine fractionation at VST-2b and VSR-3, respectively; purple/orange lines = best-fitting concentrations calculated by inverse modeling using melt fraction distribution as function of depth shown in panel (b). Values of ϵ_{Nd} are taken from Pearman et al. (2026). Note that VST-2b is modeled using $\epsilon_{Nd} = 1$. (b) Purple/orange lines with bands = optimal melt fractions as function of depth for VST-2b and VSR-3 obtained by minimizing misfit between observed and calculated rare earth element concentrations shown in panel (a) where width of each band represents uncertainty obtained by *Monte Carlo* modeling with 1000 iterations; dark/light gray dotted lines with temperature labels = melt fractions as function of depth and temperature calculated exploiting approach described by McKenzie (1984) and by Katz et al. (2003) with revised parameters from Shorttle et al. (2014) where dark/light gray lines are calculated for $H_2O = 0.014$ and 0.034 wt.%, respectively; vertical dotted lines = garnet-spinel transition (69–78 km) taken from Tomlinson and Holland (2021); gray rectangle along left-hand side = observed thicknesses of oceanic crust whose bases represent top of melting column where solid/dashed lines are assumed bases of crust for VST-2b (8.6 km) and VSR-3 (10.4 km), respectively (Poore et al., 2011). (c, d) Observed and calculated concentrations of other major, minor and trace elements where calculated concentrations are obtained by forward modeling using melt fractions as function of depth recovered by inverting rare earth element concentrations. (e–h) Geochemical modeling of VST-2b and of VSR-3 assuming crustal thicknesses of 8.6 and 10.4 km together with melting paths, respectively (Figure 8b). In panel (f), dark/light gray isothermal profiles are calculated for $H_2O = 0.011$ and 0.028 wt.%, respectively. Note that these constraints predicate mantle source compositions shown in Figure 7a. (i–l) Geochemical modeling of VST-2b and of VSR-3 assuming ϵ_{Nd} values of 7.81 and 10.22, respectively. In panel (j), dark/light gray isothermal profiles are calculated for $H_2O = 0.011$ and 0.014 wt.%, respectively.

not intended to exclude other possibilities—they are meant to be illustrative. In the first model, we require melt fraction as a function of depth to track a constant isentropic temperature. This requirement is a reasonable expectation since inverse modeling of both the zero-age and young troughs yields constant temperatures. In the case of the old trough, we find that major element, trace element and REE concentrations can be only be fitted if we disregard the binary source calculated using $\epsilon_{Nd} = 7.81$ and use a mantle source that dominated by, say, the PM end-member which can be simulated by assuming $\epsilon_{Nd} = 1.0$. *Monte Carlo* inverse modeling yields a melt fraction with depth that is consistent with a mantle temperature of 1400°C. Unfortunately, the cumulative melt thickness is 15.0 km which is undoubtedly too great, given that the residual depth anomaly at this location is consistent with a much thinner ocean crust (i.e., <10 km). The calculated melt profile reflects the fact that heavy REE concentrations are lower than for the zero-age and young troughs.

In the second model, we use a combination of forward and inverse modeling to calculate the mantle source composition that is required if the melting profile is consistent with a temperature of 1350°C, which yields a cumulative melt thickness of 8.6 km (i.e., the same as that obtained for the zero-age and young troughs). Once again, we find that major, trace and REE concentrations can be fitted provided the mantle source composition is that shown in Figure 7a. This calculated source composition has two important features. It is very enriched at the light REE end but, critically, depleted at the heavy REE end. Both features contribute to the ability to match observed REE concentrations for a melting profile that is consistent with what was determined for the other troughs. This mantle source cannot be constructed by simple binary mixing between PM and DM. Instead, it

requires an additional source component which could conceivably be garnet pyroxenite with a trace element composition that is determined from a mixture of DM and recycled MORB (Stracke et al., 2000).

In the third model, we seek the optimal melt fraction distribution as a function of depth for a mantle source whose composition is constructed by binary mixing of PM and DM end-members using $\epsilon_{Nd} = 7.81$ (McDonough & Sun, 1995). In this case, we can only match observed and calculated REE concentrations if the melt fraction as a function of depth has a long tail between 50 and 180 km (Figure 9j). The existence of this tail ensures that melting takes place in the presence of garnet which acts to depress the concentrations of heavy REEs. The presence of a melting tail therefore has almost precisely the same effect as the calculated mantle source used in the second model.

Our modeling strategy for the old ridge is closely similar (Figure 9). Since $\epsilon_{Nd} = 8.02$, the mantle source is not expected to be quite as enriched as for the old trough, which probably accounts for much of the disparity in concentrations of light REEs. *Monte Carlo* inverse modeling yields a good fit between observed and calculated REE concentrations. Major, minor and trace element concentrations are also matched (Figures 9c and 9d). The recovered melt fraction as a function of depth shares the same characteristics as those recovered for the zero-age and young ridges—a higher average temperature than for the adjacent trough and suppression of melting at depth. However, the cumulative melt thickness is 16.4 km, which is significantly thicker than expected. In the second model, the melting profile is fixed to yield a melt thickness of 11.0 km. The calculated mantle source which is required to minimize the misfit between observed and calculated REE concentrations is shown in Figure 7a. At the light REE end, this calculated source is almost identical to the DM end-member based upon Workman and Hart (2005). At the heavy REE end, it is slightly more depleted than the source calculated for the old trough. In the third model, *Monte Carlo* inverse modeling is carried out by assuming the more depleted DM source (i.e., $\epsilon_{Nd} = 10.22$). In this case, the recovered melting profile is consistent with an average mantle temperature that just exceeds 1400°C and generates a cumulative melt thickness of 14.5 km (Figure 9j). There is a small melting tail which extends to a depth of ∼120 km and has mantle source implications.

We readily acknowledge that geochemical modeling of this ridge-trough pair is not straightforward due to undoubted mantle source complexity. Nevertheless, the modeling possibilities presented here still imply that mantle temperature plays a central role in determining cumulative melt thickness. It is also reasonable to assume that the suite of V-shaped ridges and troughs has a common origin. Future models can build upon this approach by investigating the effects of variable mantle source composition that pays closer attention to constraints from Iceland itself.

5. Discussion

Combined forward and inverse modeling of major, trace and rare earth elements from three pairs of V-shaped ridges and troughs has yielded two sets of results which provide significant insight into the geodynamical evolution of the Icelandic Plume (Table 6). First of all, the actively forming V-shaped trough-ridge pair, VST-1 and VSR-1, at the Reykjanes Ridge appear to have formed as a consequence of small (25–30°C) temperature fluctuations. In order to account for the diachroneity of ridges and troughs, these fluctuations must horizontally advect (either linearly or radially) away from a putative plume conduit. Thus temperature variations appear to control key differences in the chemical composition of dredged basaltic glasses and rocks which are formed by melting of a depleted mantle source. Immediately off axis, a slightly older (i.e., 2.8 Myrs) manifestation of the same trough, VST-1, and the next oldest (i.e., 5.2 Myrs) ridge, VSR-2a, appear to have formed in a closely similar way, albeit by melting a marginally more enriched mantle source based upon a slightly reduced value of ϵ_{Nd}. The drilled whole-rock analyses from this young trough-ridge pair also indicate that the mantle source of the ridge is fractionally more enriched than the adjacent trough, as is the case for the zero-age pair. It is important to emphasize that significant variation in H_2O content of the mantle source do not affect our modeling result.

Second, and in contrast, the next trough-ridge pair, which are 12.7 and 13.9 Myrs old, have a less straightforward geochemical history. In each case, ϵ_{Nd} is significantly lower than expected at this radial distance from the plume center (7.81 and 8.02, respectively). These values indicate that their mantle sources consist of a mixture of DM and PM end-members as is found at the shallow northern end of the Reykjanes Ridge and its onshore expression. Furthermore, whole-rock analyses demonstrate that basalts from the trough are considerably more enriched than basalts from the ridge. This enrichment is particularly marked for light REEs and for large ion lithophiles as well as for Ti, Nb and Ta. Despite these compositional differences, the chemistry of this older trough-ridge pair are best

Table 6
Summary of Results

Hole	Location	Latitude	Longitude	WD(km)	Δz(m)	Δg(mgal)	ϵ_{Nd}	H_2O (ppm)	$\int Fdz$(km)	T_p(°C)
Axis	VST-1	58° 37.326′N	31° 25.308′W	1.48	0	−12	10.22	150	8.61	1343 ± 3
Axis	VSR-1	60° 17.532′N	29° 01.110′W	0.85	300	+14	10.20	170	10.94	1370 ± 3
U1555G	VST-1	60° 13.6849′N	28° 29.9997′W	1.52	0	−8	9.80	160	9.13	1343 ± 3
U1555I	VST-1	60° 13.6897′N	28° 29.9984′W	1.52	0	−8	9.80	160	9.13	1343 ± 3
U1563B	VSR-2a	60° 11.9946′N	27° 59.9996′W	1.42	200	10	9.42	160	12.06	1383 ± 3
U1554F	VST-2b	60° 07.5136′N	26° 42.1140′W	1.87	150	−6	7.81	280	8.63	1340 ± 3
U1562B	VSR-3	60° 06.2993′N	26° 30.1026′W	2.00	50	6	8.02	110	10.96	1373 ± 3

explained by differences in melt fraction as a function of depth which reflect similarly small temperature fluctuations. The lower value of ϵ_{Nd} can be explained by an increase in plume flux which is consistent with the greater propagation velocity of VSR-3 compared with younger VSRs (Figures 2 and 7). Plume flux variation is discussed in greater detail by Poore et al. (2009) and by Parnell-Turner et al. (2017).

It is difficult to envisage how these observational results can be accounted for by alternative hypotheses such as ridge-centric rift propagation effects, which undoubtedly occur much closer to Iceland itself, or wet melting associated with buoyant mantle cells that do not laterally advect (Hey et al., 2010; Martinez & Hey, 2017). An important way to independently test our observational results is to exploit the relationship between mantle temperature and thickness measurements of oceanic crust at V-shaped ridges and troughs (Smallwood et al., 1995). At present, there exist a small number of crustal thickness measurements that are determined using the results of seismic wide-angle experiments along and adjacent to the Reykjanes Ridge (Jones et al., 2014; Navin et al., 1998; Smallwood et al., 1995). In the current absence of crustal thickness measurements along the flowline and building upon the approach of Parnell-Turner et al. (2017), we exploit residual depth measurements calculated from the varying depth to the sediment-basement interface to estimate T_p, the mantle potential temperature where

$$T_p \approx 16\left[t_c + \left(\frac{\rho_a - \rho_w}{\rho_a - \rho_c}\right)\Delta z\right] + 1200 \tag{4}$$

where $\rho_a = 3.2$ Mg m^{-3} is the density of the asthenosphere, $\rho_c = 2.8$ Mg m^{-3} is the density of oceanic crust, and $\rho_w = 1.0$ Mg m^{-3} is the density of water. In this empirical relationship, $t_c = 8.6$ km is used as a reference crustal thickness equivalent to $T_p = 1350$°C for a residual depth, $\Delta z = 0$ km. In this way, we convert residual depth measurements into temperatures northward along the mid-oceanic ridge up to 60°N and thence eastward along the intersecting flowline. These geophysically determined temperatures can be directly compared with geochemically determined temperatures (Figure 10a). Our results show that there is a reasonable agreement between these different temperature estimates which accords with the general understanding of the extent and temperature structure of the Icelandic Plume (see, e.g., Ito, 2001; R. White & McKenzie, 1989).

From the perspective of other geochemical modeling approaches, we emphasize that our modeling strategy embraces various proxies (both single element and ratios) which are often used to characterize mantle processes (Figures 10b–10e). For example, it is well known that a global inventory of $Na_{8.0}$ measurements inversely correlate with mid-oceanic ridge depth (Gale et al., 2014). This excellent correlation can be used to infer mantle temperatures using modeling methods that complement the polybaric, multi-elemental approach taken here. In Figure 10c, our observed values of $NaO_{8.0}$ lie at the lower end of this empirical relationship which confirms that sub-plate temperatures are elevated.

From simple isostatic considerations, the relationship between mantle temperature, T_1, and anomalous ridge depth, S_1, is given by

$$T_1 = \frac{(S_0 - S_1)(\rho_m - \rho_w) + (t_{c0} - t_{c1})(\rho_m - \rho_c) + \rho_m \alpha T_0 (a - t_{c0})}{\rho_m \alpha (S_0 - S_1 + a + t_{c1})}. \tag{5}$$

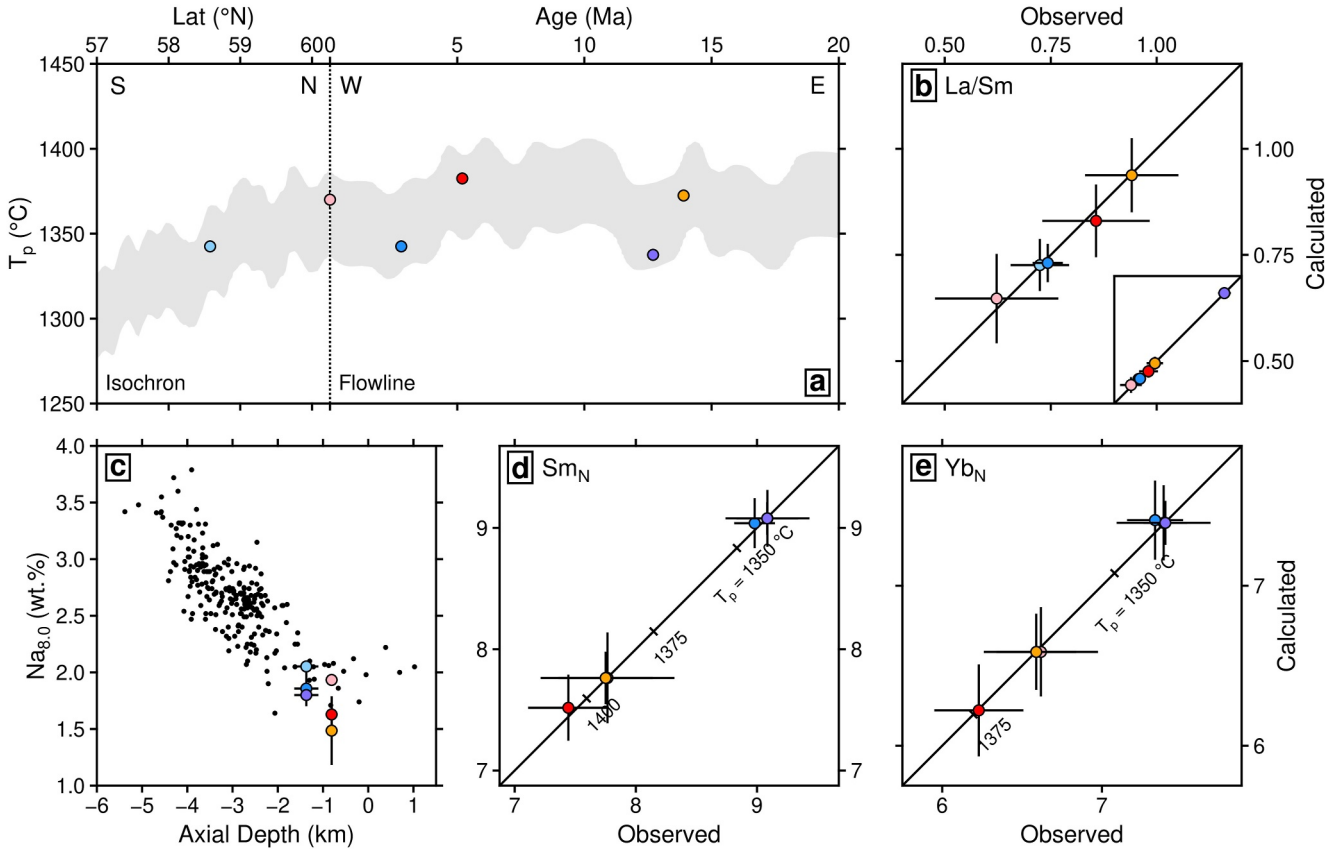

Figure 10. Further Tests of Geochemical Results. (a) Mantle potential temperature, T_p, plotted as function of distance along portion of Reykjanes Ridge (labeled S to N) and as function of age along portion of flowline taken from Parnell-Turner et al. (2017) and labeled W to E. Colored circles = geochemical estimates of T_p where uncertainties determined by inverse modeling are smaller than circle diameters (see Figures 8 and 9); gray band = geophysical estimates of T_p calculated from bathymetry of Reykjanes Ridge along S-N portion and from residual depth to oceanic basement measurements along W-E portion; dotted line = boundary between two portions. (b) Colored circles = five observed and calculated values of La/Sm; inset panel shows all six values with axial range of 0.4–2.1. (c) $Na_{8.0}$ plotted as function of axial depth. Black points = global database of values (Gale et al., 2014); colored circles with vertical lines = calculated values of $Na_{8.0}$ and their uncertainties from this study (see Figures 8 and 9). (d) Colored circles = observed and calculated values of Sm_N where N refers to normalization with respect to mantle source. 45° line shows estimated values of T_p assuming adiabatic melting. (e) Same for Yb_N.

$S_0 = 2.5$ km is the average ridge depth, $(\rho_m - \rho_w) = 2.33$ Mg m^{-3} is the difference between the densities of mantle and water, $(\rho_m - \rho_c) = 0.53$ Mg m^{-3} is the difference between the densities of mantle and crust, $\alpha = 3 \times 10^{-5}$°C^{-1} is the thermal expansion coefficient, $t_{c0} = 6.5$ km is the reference crustal thickness of average depth, t_{c1} is the crustal thickness at the location with anomalous ridge depth, and $a = 200$ km is the depth to the base of the plume layer. At the zero-age trough where $S_1 = 1.6$ km and $t_{c1} = 8.6$ km, we obtain $T_1 = 1363$°C. At the zero-age ridge where $S_1 = 0.94$ km and $t_{c1} = 10.4$ km, we obtain $T_1 = 1380$°C. Both values are consistent with the modeled geochemical results. These empirical observations are bolstered by examining observed and calculated values of heavy REEs such as Sm and Yb (Figures 10d and 10e). The match in both cases is satisfactory. Furthermore, the calculated temperatures for V-shaped ridges and troughs separate out in a systematic and predictable way.

From a more general perspective, these modeling results might help to constrain the evolving geometry of the melting column during putative radial spreading within the Icelandic Plume (Figure 11). At each V-shaped trough, recovered melt fractions as a function of depth are consistent with adiabatic decompression of mantle rocks using a constant isentropic temperature of ~1350°C. At each V-shaped ridge, recovered melt fractions show that little melt is extracted from the bottom 20 km of the melting columns (Figures 8b, 8f, and 9f). This exclusion is justified given the likely shape of the melting region that generates V-shaped ridges (Figure 11a). We envisage a pulse of hot asthenosphere spreading radially away from the plume conduit beneath Iceland. Its cross-sectional

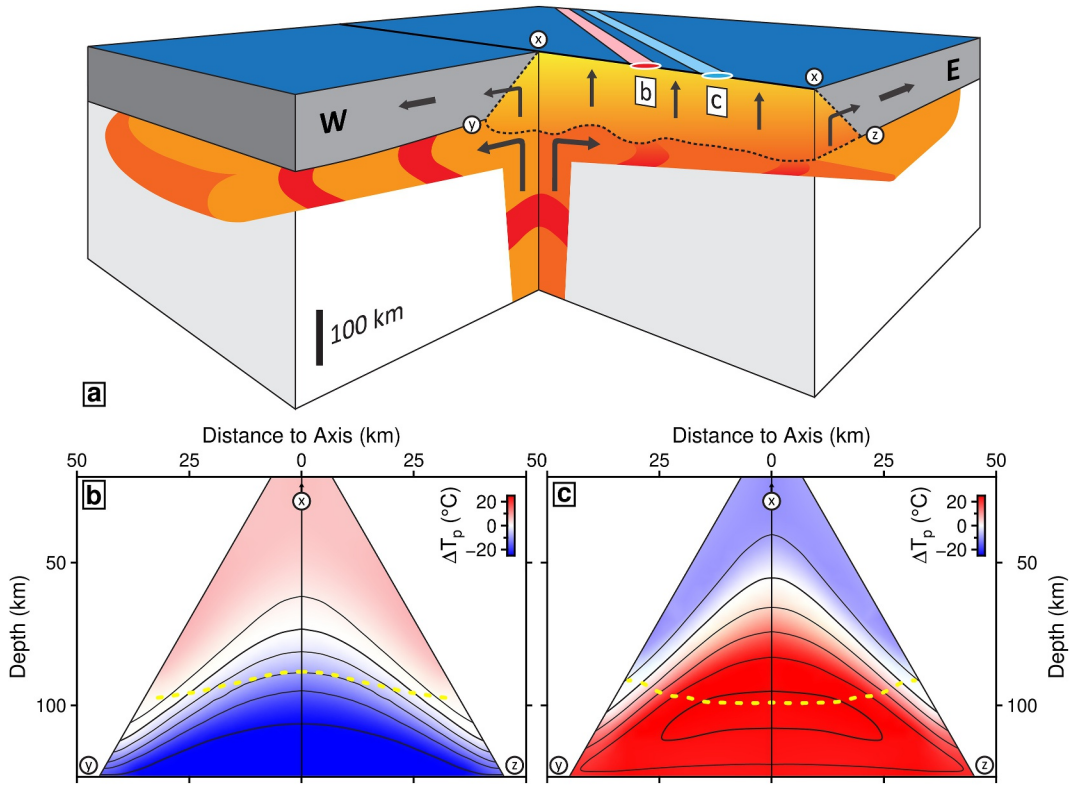

Figure 11. Schematic Structure of Icelandic Plume. (a) Cutaway cartoon showing geometry of Icelandic Plume. Orange body = plume material flowing beneath lithosphere; red patches = blobs of hotter-than-average material which expand radially outwards by Poiseuille flow; blue and gray block = lithosphere; black line = Reykjanes Ridge that straddles plume; red and blue circles and strips represent surface projections of V-shaped ridge (above blob) and trough (above no blob); cut-away orange prism labeled x-y-z = melting region below ridge under which hot annuli of plume material travel where letters (b, c) show positions of triangular cross-sections shown in panels b and c; black arrows indicate plate motion, plume flow, and corner flow within melting region. (b, c) Snapshots of calculated temperature structure within triangular cross-sections of prism, whose positions are shown in panel (a), redrawn from Jones et al. (2014). In each case, yellow dashed line indicates onset of melting.

geometry is parabolic and governed by Poiseuille flow (Rudge et al., 2008). Along the ridge axis, the upper half of this pulse traverses the melting region, generating chemically depleted melts. Colder (but depleted) asthenosphere rises in the wake of this pulse and suppresses the generation of melt at the base of the melting region. In Jones et al. (2014), these ideas are used to calculate the temperature structure at a mid-oceanic ridge by assuming that a hot pulse of material is advected by corner flow into the melting region (Figures 11b and 11c). The two-component velocity field calculations yield snapshots of the melting region that are consistent with our geochemical modeling results.

6. Conclusions

We present and analyze major, trace and rare earth element measurements from V-shaped ridges and troughs that flank the Reykjanes Ridge south of Iceland. These measurements have been quantitatively modeled using a polybaric fractional melting scheme which calculates the optimal melting profile that yields the best fit between observed and calculated REE concentrations. A combination of inverse and forward modeling demonstrates that V-shaped ridges and troughs are geochemically and thermally distinct. While variations in mantle source composition play a role in determining major, minor, trace and rare earth element concentrations, we show that resolvable temperature differences predominate that appear to rule out alternative hypotheses such as rift propagation effects and buoyant wet mantle cells. There are two significant results. First, the temperature differences within the mantle source beneath ridges and troughs are 25–30°C which agree with inferences made from oceanic crustal thickness measurements (R. S. White et al., 1995). Second, the detailed structure of melting profiles

beneath ridges and troughs differ—melting is suppressed toward the base of the melting column beneath ridges which could be consistent with radial Poiseuille flow of a hot pulse of material. In future, a closer combination of geochemical and geophysical studies south of Iceland should yield fruitful insights.

Appendix A

Anne Briais[1], Sidney R. Hemming[2,3], Leah J. LeVay[4], Tom Dunkley Jones[5], Ying Cui[6], Anita Di Chiara[7], Justin P. Dodd[8], Deepa Dwyer[9], Deborah E. Eason[10], Sarah A. Friedman[11], Katharina Hochmuth[12], Halima E. Ibrahim[13], Claire E. Jasper[14,15,16], Boris-Theofanis Karatsolis[17,18], Saran Lee-Takeda[19], Danielle E. LeBlanc[20], Melody R. Lindsay[21], David D. McNamara[22], Sevasti E. Modestou[23], Margaret A. Morris[24], Bramley J. Murton[25], Suzanne O'Connell[26], Gabriel Pasquet[27,28], Paul N. Pearson[29], Sheng-Ping Qian[30], Yair Rosenthal[31], Sara Satolli[32], Matthias Sinnesael[33], Takuma Suzuki[34], Thena Thulasi[35], Nicky White[36], Tao Wu[37], Alexandra Y. Yang[38], Ross Parnell-Turner[24], Callum Pearman[36], Chia-Yu Tien[36], Viviane dos Santos Rocha[39]

[1]Geo-Ocean, Centre National de la Recherche Scientifique (CNRS), Institut Universitaire Européen de la Mer, Rue Dumont d'Urville, Plouzané, France, [2]Department of Earth and Environmental Sciences, Columbia University, New York, NY, USA, [3]Lamont-Doherty Earth Observatory, Columbia University, Palisades, NY, USA, [4]International Ocean Discovery Program, Texas A&M University, College Station, TX, USA, [5]School of Geography, Earth and Environmental Sciences, University of Birmingham, Birmingham, UK, [6]Department of Earth and Environmental Studies, Montclair State University, Montclair, NJ, USA, [7]Istituto Nazionale di Geofisica e Vulcanologia, Roma, Italy, [8]Department of Oceanography, Texas A&M University, College Station, TX, USA, [9]College of Earth Ocean and Atmospheric Sciences, Oregon State University, Corvallis, OR, USA, [10]Department of Earth Sciences, School of Ocean & Earth Science & Technology, University of Hawai'i at Mānoa, Honolulu, HI, USA, [11]School of Earth, Environment & Sustainability, Georgia Southern University, Statesboro, GA, USA, [12]Institute of Marine and Antarctic Studies (IMAS), College of Science and Engineering, University of Tasmania, Hobart, TAS, Australia, [13]Department of Earth Sciences Binghamton University, Binghamton, NY, USA, [14]Now at Ocean Sciences Department, University of California, Santa Cruz, Santa Cruz, CA, USA, [15]Department of Earth and Environmental Sciences, Columbia University, New York, NY, USA, [16]Lamont-Doherty Earth Observatory, Columbia University, Palisades, NY, USA, [17]Department of Earth Sciences, Uppsala University, Uppsala, Sweden, [18]Now at Department of Geosciences, University of Fribourg, Fribourg, Switzerland, [19]Atmosphere and Ocean Research Institute, The University of Tokyo, Kashiwa, Chiba, Japan, [20]Woods Hole Oceanographic Institution, Woods Hole, MA, USA, [21]Bigelow Laboratory for Ocean Sciences, East Boothbay, ME, USA, [22]Department of Earth, Ocean and Ecological Sciences, University of Liverpool, Liverpool, UK, [23]Department of Geography and Environmental Sciences, Northumbria University, Newcastle upon Tyne, UK, [24]Institute of Geophysics & Planetary Physics, Scripps Institution of Oceanography, University of California, San Diego, La Jolla, CA, USA, [25]Ocean Bio-Geoscience Group, National Oceanography Centre, Southampton, UK, [26]Department of Earth and Environmental Sciences, Wesleyan University, Middletown, CT, USA. [27]Complex Fluids and Reservoirs Laboratory, University of Pau and Pays de l'Adour, Avenue De l'Université, Pau, France, [28]Now at Bureau of Economic Geology, Jackson School of Geosciences, The University of Texas at Austin, Austin, TX, USA, [29]Department of Earth Sciences, University College London, London, UK, [30]Southern Marine Science and Engineering Guangdong Laboratory (Guangzhou), Guangzhou, China, [31]Department of Marine and Coastal Sciences, Rutgers, The State University of New Jersey, New Brunswick, NJ, USA, [32]Department of Engineering and Geology, University of Chieti-Pescara, Chieti, Italy, [33]Geology, School of Natural Sciences, Trinity College Dublin, The University of Dublin, Dublin, Ireland, [34]SUGAR, X-star, Japan Agency for Marine-Earth Science and Technology (JAMSTEC), Yokosuka, Japan, [35]Geosciences Division, National Centre for Polar and Ocean Research (NCPOR), Vasco-da-Gama, Goa, India, [36]Bullard Laboratories, Department of Earth Sciences, University of Cambridge, Cambridge, UK, [37]Ocean College, Zhejiang University, Zhoushan, China, [38]Guangzhou Institute of Geochemistry, Chinese Academy of Sciences, Guangzhou, China, [39]Earth, Atmosphere and Environment, Northern Illinois University, DeKalb, IL, USA

Conflict of Interest

The authors declare no conflicts of interest relevant to this study.

Availability Statement

The data described in this study have been archived at Mendeley Data and are publicly available from Tien (2026). The INVMEL software package is freely available from D. McKenzie (mckenzie@madingley.org).

Acknowledgments
This research used samples and data provided by the International Ocean Discovery Program (IODP). Funding was provided by the Natural Environment Research Council (NERC) and by IODP. We thank the JOIDES Resolution Science Operator technical staff and crew of the JOIDES Resolution who sailed on Expeditions 384, 395C, and 395 for their professional expertise during and following the COVID-19 pandemic event. This paper is dedicated to J. P. B. Lovell who would have been most pleased. We are grateful to J. Day, G. Calder, G. Fitton, S. Gibson, D. McKenzie and J. Rudge for their help. P. Asimow and D. Geist provided helpful guidance and review. Department of Earth Sciences contribution number esc.120430.

References

Abelson, M., Agnon, A., & Almogi-Labin, A. (2008). Indications for control of the Iceland plume on the Eocene–Oligocene "greenhouse–icehouse" climate transition. *Earth and Planetary Science Letters*, *265*(1–2), 33–48. https://doi.org/10.1016/j.epsl.2007.09.021

Amante, C., & Eakins, B. W. (2009). ETOPO1 arc-minute global relief model: Procedures, data sources and analysis. https://doi.org/10.7289/V5C8276M

Ball, P. W., White, N. J., Maclennan, J., & Stephenson, S. N. (2021). Global influence of mantle temperature and plate thickness on intraplate volcanism. *Nature Communications*, *12*(1), 2045. https://doi.org/10.1038/s41467-021-22323-9

Blichert-Toft, J., Agranier, A., Andres, M., Kingsley, R., Schilling, J.-G., & Albarède, F. (2005). Geochemical segmentation of the Mid-Atlantic Ridge north of Iceland and ridge–hot spot interaction in the North Atlantic. *Geochemistry, Geophysics, Geosystems*, *6*(1). https://doi.org/10.1029/2004GC000788

Blundy, J., & Wood, B. (2003). Partitioning of trace elements between crystals and melts. *Earth and Planetary Science Letters*, *210*(3–4), 383–397. https://doi.org/10.1016/S0012-821X(03)00129-8

Brounce, M. N., Kelley, K. A., & Cottrell, E. (2014). Variations in $Fe^{3+}/\Sigma Fe$ of Mariana arc basalts and mantle wedge fO_2. *Journal of Petrology*, *55*(12), 2513–2536. https://doi.org/10.1093/petrology/egu065

Conway-Jones, B. W., & White, N. (2022). Paleogene buried landscapes and climatic aberrations triggered by mantle plume activity. *Earth and Planetary Science Letters*, *593*, 117644. https://doi.org/10.1016/j.epsl.2022.117644

Cottrell, E., & Kelley, K. A. (2011). The oxidation state of Fe in MORB glasses and the oxygen fugacity of the upper mantle. *Earth and Planetary Science Letters*, *305*(3–4), 270–282. https://doi.org/10.1016/j.epsl.2011.03.014

Dixon, J. E., Leist, L., Langmuir, C., & Schilling, J.-G. (2002). Recycled dehydrated lithosphere observed in plume-influenced mid-ocean ridge basalt. *Nature*, *420*(6914), 385–389. https://doi.org/10.1038/nature01215

Engdahl, E. R., Di Giacomo, D., Sakarya, B., Gkarlaouni, C. G., Harris, J., & Storchak, D. A. (2020). ISC-EHB 1964–2016, an improved data set for studies of Earth structure and global seismicity. *Earth and Space Science*, *7*(1), e2019EA000897. https://doi.org/10.1029/2019EA000897

Fitton, J. G., Saunders, A. D., Larsen, L. M., Hardarson, B. S., & Norry, M. J. (1998). *Volcanic rocks from the southeast Greenland margin at 63°N: Composition, petrogenesis, and mantle sources* (Technical Report). Ocean Drilling Program. https://doi.org/10.2973/odp.proc.sr.152.233.1998

Gale, A., Dalton, C. A., Langmuir, C. H., Su, Y., & Schilling, J.-G. (2013). The mean composition of ocean ridge basalts. *Geochemistry, Geophysics, Geosystems*, *14*(3), 489–518. https://doi.org/10.1029/2012GC004334

Gale, A., Langmuir, C. H., & Dalton, C. A. (2014). The global systematics of ocean ridge basalts and their origin. *Journal of Petrology*, *55*(6), 1051–1082. https://doi.org/10.1093/petrology/egu017

Gibson, S. A., & Geist, D. (2010). Geochemical and geophysical estimates of lithospheric thickness variation beneath Galápagos. *Earth and Planetary Science Letters*, *300*(3), 275–286. https://doi.org/10.1016/j.epsl.2010.10.002

Gibson, S. A., Thompson, R. N., Day, J. A., Humphris, S. E., & Dickin, A. P. (2005). Melt-generation processes associated with the Tristan mantle plume: Constraints on the origin of EM-1. *Earth and Planetary Science Letters*, *237*(3–4), 744–767. https://doi.org/10.1016/j.epsl.2005.06.015

Hey, R., Martinez, F., Höskuldsson, Á., & Benediktsdóttir, Á. (2010). Propagating rift model for the V-shaped ridges south of Iceland. *Geochemistry, Geophysics, Geosystems*, *11*(3). https://doi.org/10.1029/2009GC002865

Hoggard, M. J., Parnell-Turner, R., & White, N. (2020). Hotspots and mantle plumes revisited: Towards reconciling the mantle heat transfer discrepancy. *Earth and Planetary Science Letters*, *542*, 116317. https://doi.org/10.1016/j.epsl.2020.116317

Irvine, T. N., & Baragar, W. R. A. (1971). A guide to the chemical classification of the common volcanic rocks. *Canadian Journal of Earth Sciences*, *8*(5), 523–548. https://doi.org/10.1139/e71-055

Ito, G. (2001). Reykjanes 'V'-shaped ridges originating from a pulsing and dehydrating mantle plume. *Nature*, *411*(6838), 681–684. https://doi.org/10.1038/35079561

Jones, S. M., Murton, B. J., Fitton, J. G., White, N. J., Maclennan, J., & Walters, R. L. (2014). A joint geochemical–geophysical record of time-dependent mantle convection south of Iceland. *Earth and Planetary Science Letters*, *386*, 86–97. https://doi.org/10.1016/j.epsl.2013.09.029

Katz, R. F., Spiegelman, M., & Langmuir, C. H. (2003). A new parameterization of hydrous mantle melting. *Geochemistry, Geophysics, Geosystems*, *4*(9), 1073. https://doi.org/10.1029/2002GC000433

Kempton, P. D., Fitton, J. G., Saunders, A. D., Nowell, G. M., Taylor, R. N., Hardarson, B. S., & Pearson, G. (2000). The Iceland plume in space and time: A Sr–Nd–Pb–Hf study of the North Atlantic rifted margin. *Earth and Planetary Science Letters*, *177*(3–4), 255–271. https://doi.org/10.1016/S0012-821X(00)00047-9

Kokfelt, T. F., Hoernle, K. A. J., Hauff, F., Fiebig, J., Werner, R., & Garbe-Schoenberg, D. (2006). Combined trace element and Pb–Nd–Sr–O isotope evidence for recycled oceanic crust (upper and lower) in the Iceland mantle plume. *Journal of Petrology*, *47*(9), 1705–1749. https://doi.org/10.1093/petrology/egl025

Lee, C.-T. A., Luffi, P., Plank, T., Dalton, H., & Leeman, W. P. (2009). Constraints on the depths and temperatures of basaltic magma generation on Earth and other terrestrial planets using new thermobarometers for mafic magmas. *Earth and Planetary Science Letters*, *279*(1–2), 20–33. https://doi.org/10.1016/j.epsl.2008.12.020

Le Maitre, R. W. (1989). A classification of igneous rocks and glossary of terms.

Martinez, F., & Hey, R. (2017). Propagating buoyant mantle upwelling on the Reykjanes Ridge. *Earth and Planetary Science Letters*, *457*, 10–22. https://doi.org/10.1016/j.epsl.2016.09.057

McDonough, W. F., & Sun, S.-S. (1995). The composition of the Earth. *Chemical Geology*, *120*(3–4), 223–253. https://doi.org/10.1016/0009-2541(94)00140-4

McKenzie, D. (1984). The generation and compaction of partially molten rock. *Journal of Petrology*, *25*(3), 713–765. https://doi.org/10.1093/petrology/25.3.713

McKenzie, D., & O'Nions, R. K. (1991). Partial melt distributions from inversion of rare earth element concentrations. *Journal of Petrology*, *32*(5), 1021–1091. https://doi.org/10.1093/petrology/32.5.1021

Michael, P. (1995). Regionally distinctive sources of depleted MORB: Evidence from trace elements and H_2O. *Earth and Planetary Science Letters*, *131*(3–4), 301–320. https://doi.org/10.1016/0012-821X(95)00023-6

Murton, B. J., Taylor, R. N., & Thirlwall, M. F. (2002). Plume–ridge interaction: A geochemical perspective from the Reykjanes Ridge. *Journal of Petrology*, *43*(11), 1987–2012. https://doi.org/10.1093/petrology/43.11.1987

Navin, D. A., Peirce, C., & Sinha, M. C. (1998). The RAMESSES experiment—II. Evidence for accumulated melt beneath a slow spreading ridge from wide-angle refraction and multichannel reflection seismic profiles. *Geophysical Journal International*, *135*(3), 746–772. https://doi.org/10.1046/j.1365-246X.1998.00709.x

Nichols, A. R. L., Carroll, M. R., & Höskuldsson, Á. (2002). Is the Iceland hot spot also wet? Evidence from the water contents of undegassed submarine and subglacial pillow basalts. *Earth and Planetary Science Letters*, *202*(1), 77–87. https://doi.org/10.1016/S0012-821X(02)00758-6

O'Nions, R. K., Evensen, N. M., & Hamilton, P. J. (1979). Geochemical modeling of mantle differentiation and crustal growth. *Journal of Geophysical Research*, *84*(B11), 6091–6101. https://doi.org/10.1029/JB084iB11p06091

Parnell-Turner, R., Briais, A., & LeVay, L. J., & the Expedition 395 Scientists. (2022). *Expedition 395C preliminary report: Reykjanes mantle convection and climate: Crustal objectives* (Technical Report). International Ocean Discovery Program. https://doi.org/10.14379/iodp.pr.395C.2022

Parnell-Turner, R., Briais, A., & LeVay, L. J., & the Expedition 395 Scientists. (2024). *Expedition 395 preliminary report: Reykjanes mantle convection and climate* (Technical Report). International Ocean Discovery Program. https://doi.org/10.14379/iodp.pr.395.2024

Parnell-Turner, R., Briais, A., & LeVay, L. J., & the Expedition 395 Scientists. (2025). *Reykjanes mantle convection and climate* (Technical Report). International Ocean Discovery Program. https://doi.org/10.14379/iodp.proc.395.2025

Parnell-Turner, R., White, N., Henstock, T., Murton, B., Maclennan, J., & Jones, S. M. (2014). A continuous 55-million-year record of transient mantle plume activity beneath Iceland. *Nature Geoscience*, *7*(12), 914–919. https://doi.org/10.1038/ngeo2281

Parnell-Turner, R., White, N., Henstock, T. J., Jones, S. M., Maclennan, J., & Murton, B. J. (2017). Causes and consequences of diachronous V-shaped ridges in the North Atlantic Ocean. *Journal of Geophysical Research: Solid Earth*, *122*(11), 8675–8708. https://doi.org/10.1002/2017JB014225

Pearman, C., Tien, C.-Y., White, N., & Maclennan, J., & IODP Expedition 395 Science Party. (2026). Ocean drilling reveals collapse and resurgence of the Iceland mantle plume. *Nature Communications*. (Manuscript under review).

Peate, D. W., Baker, J. A., Jakobsson, S. P., Waight, T. E., Kent, A. J. R., Grassineau, N. V., & Skovgaard, A. C. (2009). Historic magmatism on the Reykjanes Peninsula, Iceland: A snap-shot of melt generation at a ridge segment. *Contributions to Mineralogy and Petrology*, *157*(3), 359–382. https://doi.org/10.1007/s00410-008-0339-4

Poore, H., Samworth, R., White, N. J., Jones, S. M., & McCave, I. N. (2006). Neogene overflow of Northern Component Water at the Greenland-Scotland Ridge. *Geochemistry, Geophysics, Geosystems*, *7*(6). https://doi.org/10.1029/2005GC001085

Poore, H., White, N., & Jones, S. (2009). A Neogene chronology of Iceland plume activity from V-shaped ridges. *Earth and Planetary Science Letters*, *283*(1–4), 1–13. https://doi.org/10.1016/j.epsl.2009.02.028

Poore, H., White, N., & Maclennan, J. (2011). Ocean circulation and mantle melting controlled by radial flow of hot pulses in the Iceland plume. *Nature Geoscience*, *4*(8), 558–561. https://doi.org/10.1038/ngeo1161

Press, W. H., Vetterling, W. T., Teukolsky, S. A., & Flannery, B. P. (1988). Numerical recipes.

Roeder, P. L., & Emslie, R. F. (1970). Olivine–liquid equilibrium. *Contributions to Mineralogy and Petrology*, *29*(4), 275–289. https://doi.org/10.1007/BF00371276

Rudge, J. F., Shaw Champion, M. E., White, N., McKenzie, D., & Lovell, B. (2008). A plume model of transient diachronous uplift at the Earth's surface. *Earth and Planetary Science Letters*, *267*(1–2), 146–160. https://doi.org/10.1016/j.epsl.2007.11.040

Salters, V. J. M., & Stracke, A. (2004). Composition of the depleted mantle. *Geochemistry, Geophysics, Geosystems*, *5*(5). https://doi.org/10.1029/2003GC000597

Sandwell, D. T., & Smith, W. H. F. (2009). Global marine gravity from retracked Geosat and ERS-1 altimetry: Ridge segmentation versus spreading rate. *Journal of Geophysical Research*, *114*(B1). https://doi.org/10.1029/2008JB006008

Schilling, J.-G. (1973). Iceland mantle plume: Geochemical study of Reykjanes Ridge. *Nature*, *242*(5400), 565–571. https://doi.org/10.1038/242565a0

Shorttle, O., & Maclennan, J. (2011). Compositional trends of Icelandic basalts: Implications for short-length scale lithological heterogeneity in mantle plumes. *Geochemistry, Geophysics, Geosystems*, *12*(11). https://doi.org/10.1029/2011GC003748

Shorttle, O., Maclennan, J., & Jones, S. M. (2010). Control of the symmetry of plume–ridge interaction by spreading ridge geometry. *Geochemistry, Geophysics, Geosystems*, *11*(7). https://doi.org/10.1029/2009GC002986

Shorttle, O., Maclennan, J., & Lambart, S. (2014). Quantifying lithological variability in the mantle. *Earth and Planetary Science Letters*, *395*, 24–40. https://doi.org/10.1016/j.epsl.2014.03.040

Shorttle, O., Moussallam, Y., Hartley, M. E., Maclennan, J., Edmonds, M., & Murton, B. J. (2015). Fe-XANES analyses of Reykjanes Ridge basalts: Implications for oceanic crust's role in the solid Earth oxygen cycle. *Earth and Planetary Science Letters*, *427*, 272–285. https://doi.org/10.1016/j.epsl.2015.07.017

Smallwood, J. R., White, R. S., & Minshull, T. A. (1995). Sea-floor spreading in the presence of the Iceland plume: The structure of the Reykjanes Ridge at 61°40′N. *Journal of the Geological Society*, *152*(6), 1023–1029. https://doi.org/10.1144/GSL.JGS.1995.152.01.24

Stracke, A., Salters, V. J. M., & Sims, K. W. W. (2000). Assessing the presence of garnet-pyroxenite in the mantle sources of basalts through combined hafnium–neodymium–thorium isotope systematics. *Geochemistry, Geophysics, Geosystems*, *1*(12), 1006. https://doi.org/10.1029/1999GC000013

Tatsumi, Y., Sakuyama, M., Fukuyama, H., & Kushiro, I. (1983). Generation of arc basalt magmas and thermal structure of the mantle wedge in subduction zones. *Journal of Geophysical Research*, *88*(B7), 5815–5825. https://doi.org/10.1029/JB088iB07p05815

Thirlwall, M. F., Gee, M. A. M., Taylor, R. N., & Murton, B. J. (2004). Mantle components in Iceland and adjacent ridges investigated using double-spike Pb isotope ratios. *Geochimica et Cosmochimica Acta*, *68*(2), 361–386. https://doi.org/10.1016/S0016-7037(03)00424-1

Tien, C.-Y. (2026). IODP-CYT-geochemical-data [Dataset]. *Mendeley Data, V1*. https://doi.org/10.17632/f48zwpjm6n.1

Tomlinson, E. L., & Holland, T. J. B. (2021). A thermodynamic model for the subsolidus evolution and melting of peridotite. *Journal of Petrology*, *62*(1), egab012. https://doi.org/10.1093/petrology/egab012

Vogt, P. R. (1971). Asthenosphere motion recorded by the ocean floor south of Iceland. *Earth and Planetary Science Letters*, *13*(1), 153–160. https://doi.org/10.1016/0012-821X(71)90118-X

White, R., & McKenzie, D. (1989). Magmatism at rift zones: The generation of volcanic continental margins and flood basalts. *Journal of Geophysical Research*, *94*(B6), 7685–7729. https://doi.org/10.1029/JB094iB06p07685

White, R. S., Bown, J. W., & Smallwood, J. R. (1995). The temperature of the Iceland Plume and origin of outward-propagating V-shaped ridges. *Journal of the Geological Society*, *152*(6), 1039–1045. https://doi.org/10.1144/GSL.JGS.1995.152.01.26

Willbold, M., & Stracke, A. (2006). Trace element composition of mantle end-members: Implications for recycling of oceanic and upper and lower continental crust. *Geochemistry, Geophysics, Geosystems*, *7*(4). https://doi.org/10.1029/2005GC001005

Workman, R. K., & Hart, S. R. (2005). Major and trace element composition of the depleted MORB mantle (DMM). *Earth and Planetary Science Letters*, *231*(1–2), 53–72. https://doi.org/10.1016/j.epsl.2004.12.005

Wright, J. D., & Miller, K. G. (1996). Control of North Atlantic Deep Water circulation by the Greenland-Scotland Ridge. *Paleoceanography*, *11*(2), 157–170. https://doi.org/10.1029/95PA03696